



1 **Title:** Top-Down Benchmark of U.S. Methane Inventories Reveals Regional Discrepancies in  
2 Activity-Based Estimates

3

4 Authors: John Worden<sup>1,2,\*</sup>, Sudhanshu Pandey<sup>1,\*</sup>, Hannah Nesser<sup>1</sup>, Kevin Bowman<sup>1</sup>, Colin  
5 Harkins<sup>4,8</sup>, Congmeng Lyu<sup>4,8</sup>, Joannes D. Maasakkers<sup>5</sup>, Deborah Gordon<sup>6</sup>, Daniel Jacob<sup>3</sup>, Lucas  
6 Estrada<sup>3</sup>, Daniel J. Varon<sup>9,3</sup>, James D. East<sup>3</sup>, Lauren Schmeisser<sup>6</sup> and Zhen Qu<sup>7</sup>

- 7 1. Jet Propulsion Laboratory, California Institute of Technology, Pasadena, California,  
8 United States  
9 2. Joint Institute for Regional Earth System Science and Engineering, University of  
10 California, Los Angeles, Los Angeles, California, United States  
11 3. Harvard University, Cambridge, Massachusetts, United States  
12 4. NOAA Chemical Sciences Laboratory, Boulder, Colorado, United States  
13 5. SRON Netherlands Institute for Space Research, Leiden, The Netherlands  
14 6. Rocky Mountain Institute, Boulder, Colorado, United States  
15 7. North Carolina State University, Raleigh, North Carolina, United States  
16 8. Cooperative Institute for Research in Environmental Sciences, University of Colorado  
17 Boulder, Boulder, Colorado, United States  
18 9. Massachusetts Institute of Technology, Cambridge, Massachusetts, United States

19 \*These authors contributed equally to the work.

20 \* Correspondence to: John Worden [jworden@g.ucla.edu](mailto:jworden@g.ucla.edu)

21

22 Abstract: Robust estimates of methane emissions are critical for understanding their impacts on  
23 atmospheric warming and air quality, and for assessing methane mitigation strategies. Gridded  
24 inventories, such as the U.S. Environmental Protection Agency’s Greenhouse Gas Inventory  
25 (EPA GHGI), the Emissions Database for Global Atmospheric Research (EDGAR 2024), and  
26 the National Oceanic and Atmospheric Administration’s Fossil Fuel Oil and Gas inventory  
27 (NOAA FOG), are constructed to evaluate large-scale emission patterns and support identifying  
28 emission mitigation priorities and prioritizing future measurements. However, substantial  
29 differences across inventories complicate such assessments. We benchmark EPA GHGI,  
30 EDGAR 2024, and NOAA FOG against flux estimates from an atmospheric inversion of  
31 Greenhouse Gases Observing Satellite (GOSAT) data from 2012 to 2020 over the Contiguous  
32 United States (CONUS). A key technical challenge is the heterogeneous sensitivity of satellite-  
33 derived fluxes, which depends on measurement uncertainty, coverage, and inversion model  
34 configuration. We account for this heterogeneity by applying an inversion operator to each



35 inventory prior to comparison with the GOSAT-based estimates. The GOSAT estimates are most  
36 sensitive to oil&gas and livestock emissions; oil and gas emissions are consistent with NOAA  
37 FOG (14.1 Tg CH<sub>4</sub> yr<sup>-1</sup> in 2015), but exceed EPA GHGI and EDGAR, particularly across Texas,  
38 Oklahoma, and Louisiana. GOSAT-based livestock emissions exceed EPA GHGI and EDGAR  
39 by 1–2 Tg CH<sub>4</sub> yr<sup>-1</sup>, with the largest differences in the Midwest and California. Despite these  
40 discrepancies, both activity and satellite based estimates show no observable trends from 2012 to  
41 2020 in fossil and livestock emissions.

42

43

## 44 **1. Introduction**

45

46 All GOSAT-derived emissions and corresponding inputs/algorithms are available at  
47 [<https://doi.org/10.5281/zenodo.15786798>].

48 Jupyter / python code at [<https://zenodo.org/records/16921536>] shows how to compare these  
49 GOSAT derived emissions to inventories.

50

51 Methane is a potent greenhouse gas that plays a significant role in atmospheric warming  
52 (Saunio et al., 2020). Methane is emitted from multiple anthropogenic sources including  
53 livestock, oil and gas exploitation, manure, rice cultivation, wastewater, solid waste, and coal  
54 mining, and from natural sources, particularly wetlands. Methane is also the main component of  
55 natural gas, a valuable global commodity that can pose economic safety risks when it leaks.  
56 Accurate and verifiable estimates of its emissions are essential for tracking progress and guiding  
57 effective mitigation strategies, and for accounting for the economic value of energy waste (IEA,  
58 2025; World Bank, 2025). Gridded methane emission inventories, such as the gridded United  
59 States Environmental Protection Agency’s Greenhouse Gas Inventory (EPA GHGI), the  
60 Emissions Database for Global Atmospheric Research 2024 release (EDGAR 2024), and the  
61 National Oceanic and Atmospheric Administration’s Fuel-based Oil and Gas inventory (NOAA  
62 FOG), are widely used for comparing sectoral emissions, primarily at the regional scale, to  
63 atmospheric data (EPA, 2021; Maasackers et al., 2023; Crippa et al., 2020, 2024; Francoeur et  
64 al., 2021, Kruskamp *et al.* 2025 [<https://zenodo.org/records/16782735>]). However,



65 discrepancies in how the inventories are generated, e.g. from emission factor assumptions,  
66 activity data, and/or spatial proxies and resolution can result in substantial variation in both the  
67 magnitude and sectoral attribution of emissions (Hristov et al. 2017; Alvarez et al., 2018;  
68 Maasakkers et al., 2021; Petrescu et al. 2024; Gordon 2025). In some cases, differences between  
69 inventories can be as large as the emissions themselves (Figure 1), complicating the evaluation  
70 of national and regional emission trends. Verification of their underlying parameterizations is  
71 often limited by spatiotemporal mismatches between empirical measurements and inventory  
72 assumptions. Moreover, differences between activity-based emissions and flux estimates based  
73 on observations combined with atmospheric modeling (e.g., top-down atmospheric inversions)  
74 can far exceed the changes inferred from the observed growth in atmospheric methane  
75 concentrations (Nisbet et al., 2019; Worden et al., 2022). As a result, tracking mitigation  
76 progress using bottom-up inventories alone could be unreliable without independent  
77 observational constraints. In addition to these uncertainties, emissions missing in the inventories  
78 pose another significant challenge. For instance, sporadic high emitters in both fossil fuel  
79 production and waste management, often caused by mechanical failures, may not be captured in  
80 traditional inventories (Cusworth et al., 2020, 2024; Sherwin et al., 2024); consequently, the  
81 magnitude of these emissions remains poorly understood.

82 To evaluate potential uncertainties in bottom-up inventories, top-down emissions  
83 estimates derived from satellite observations, such as those from the Greenhouse Gases  
84 Observing Satellite (GOSAT), provide a valuable, independent constraint. These atmospheric  
85 measurements inherently capture all emissions influencing methane concentrations, including  
86 unreported or underestimated sources, and therefore offer a more comprehensive view of total  
87 methane emissions. However, the resulting estimates and their information content (spatial  
88 resolution + uncertainties) depend strongly on the observational sampling, sensitivity of the  
89 observation to the emissions, choice of a priori fluxes, and the inversion regularization.  
90 Consequently, over regions with limited sampling, e.g., due to clouds or low sunlight, top-down  
91 analyses have greatly reduced sensitivity to nearby emissions, so the estimates there simply  
92 reflect the *a priori*. In contrast, emissions inferred for regions with ample sampling are more  
93 likely to accurately represent local sources. The focus of this paper is to demonstrate how this  
94 GOSAT-based benchmark can be used to evaluate alternative gridded inventories while  
95 accounting for its variable information content as discussed next.



96

## 97 **Method and Data**

98 **Accounting for choice of *a priori* and inversion regularization:** Comparisons between  
99 satellite-based top-down fluxes and activity-based inventories must account for the variation in  
100 sensitivity of the data to emissions and choice of *a priori*, otherwise substantial uncertainty (also  
101 known as *smoothing error*) is introduced into the comparison (Rodgers, 2000; Worden et al.,  
102 2022, 2023). Smoothing error in this context can be mitigated for these comparisons by at least  
103 three ways: 1) by using the inventory as the *a priori* in the inversion or 2) by applying an  
104 inversion operator to the inventory being compared (the inversion operator depends on the  
105 inversion *a priori* and what is called the averaging kernel matrix, Appendix B) or 3) by adjusting  
106 the GOSAT based estimate using the gridded inventory and the averaging kernel matrix to  
107 replace the effect of the original prior (also known as prior swapping).

108 In the first scenario, recalculating the inversion and subsequently comparing to the *a*  
109 *priori* is computationally expensive (e.g., Nesser et al., 2024 and references therein) as it  
110 involves minimizing a cost function of gridded emissions vector (e.g.  $\mathbf{z}$ ) that typically has the  
111 following form:

$$112 \quad \mathbf{C} = \|\mathbf{y} - \mathbf{F}(\mathbf{z}_A)\|_{\mathbf{S}_n}^2 + \|\mathbf{z} - \mathbf{z}_A\|_{\mathbf{S}_A}^2 \quad (1)$$

113 Where  $\mathbf{y}$  is a state vector representing concentrations (e.g. total column methane or  $\text{XCH}_4$ ), the  
114 forward model  $\mathbf{F}(\mathbf{z}_A)$  in this case is the Goddard Earth Observing System – Chemistry model  
115 (GEOS-Chem) driven by a distribution of *a priori* emissions ( $\mathbf{z}_A$ ). The matrix  $\mathbf{S}_n$  represents the  
116 measurement error covariance for the total column data and the matrix  $\mathbf{S}_A$  represents the  
117 uncertainty (or covariance) in our *a priori* emissions. For the benchmark described in this paper,  
118 the vector  $\mathbf{z}$  represents the spatial distribution of anthropogenic emissions by sector, in this case  
119 livestock, waste, coal, rice, oil&gas. Wetlands and fire emissions are also estimated with the  
120 GOSAT data and the effect of jointly estimating these emissions are included in the posterior  
121 covariance and uncertainties of the anthropogenic emissions estimate (Worden *et al.* 2022;  
122 2023).



123 The estimate for the converged solution,  $\hat{\mathbf{z}}$ , can be related to the “true distribution” of the  
124 emissions ( $\mathbf{z}$ ) with the following (e.g. Rodgers 2000).

$$125 \quad \hat{\mathbf{z}} = \mathbf{z}_A + \mathbf{A}(\mathbf{z} - \mathbf{z}_A) \quad (2)$$

126

127 where for clarity we have not included the uncertainty terms (see Appendix B). The averaging  
128 kernel matrix  $\mathbf{A}$  is a function of the *a priori* and posterior covariance,  $\hat{\mathbf{Z}}$  and  $\mathbf{Z}_A$  (see Appendix B  
129 for a description of uncertainties and prior covariances) and describes the sensitivity of the  
130 distribution of estimated emissions to the true state ( $\mathbf{A} = \frac{\partial \hat{\mathbf{z}}}{\partial \mathbf{z}}$ ). Approach #2, which is to apply an  
131 inversion operator to the inventory, is equivalent to replacing  $\mathbf{z}$ , or the “true distribution” of  
132 emissions, with the alternative inventory,  $\mathbf{z}_I$  in Equation 1; this approach is commonly used for  
133 data assimilation or for comparing atmospheric trace gas profiles from models or in situ  
134 measurements to remotely sensed measurements (e.g. Wecht *et al.* 2014, Herman *et al.* 2014).  
135 This revised estimate can be compared to  $\hat{\mathbf{z}}$  while accounting for the *a priori* and regularization  
136 choices made in the inversion described by Equation 1. Approach #3 (or prior swapping) instead  
137 involves replacing  $\mathbf{z}_A$  with the alternative inventory (e.g. Rodgers and Connor 2003)

138

$$139 \quad \hat{\mathbf{z}}_{new} = \hat{\mathbf{z}} - (\mathbf{I} - \mathbf{A})\mathbf{z}_A + (\mathbf{I} - \mathbf{A})\mathbf{z}_I \quad (3)$$

140 And is equivalent to re-running the inversion described by Equation (1) with this alternative *a*  
141 *priori*.

142 As approaches 2 and 3 are linear operations, they result in equivalent comparative differences as  
143 shown in Appendix B. In this manuscript we use the inversion operator approach (Equation 2)  
144 for consistency with previous publications (e.g. Worden *et al.* 2022; 2023).

145 **Sector Based Attribution:** We use estimates of gridded integrated fluxes from a GEOS-Chem  
146 based inversion using GOSAT XCH<sub>4</sub> data as described in Qu *et al.* (2022,2024). We use a  
147 Bayesian-based sectoral partitioning approach (Appendix A, Worden *et al.*, 2022, 2023) to  
148 project these top-down integrated fluxes to emissions by sector at a 1° × 1° resolution. This  
149 approach characterizes the inversion solution by providing a posterior covariance for the solution  
150 and provides the “inversion operator” (Equation 2) that, when applied to a gridded inventory,



151 enables the comparison to inversion results by capturing the influence of the inversion's prior  
152 emissions and the sensitivity of the satellite observations to those emissions (Rodgers, 2000).  
153

154 **Inventories:** (See Appendix C for more detail) The inventories we compare include EDGAR  
155 2024 (Crippa et al. 2024), the EPA based Greenhouse Gas Inventory (GHGI) (Maasackers et al.  
156 2023), and NOAA FOG (Francoeur et al. 2021). The EDGAR and GHGI inventories provide  
157 information about methane emissions across multiple sectors (e.g., livestock, waste, oil and gas,  
158 coal, rice). The approaches estimating these emissions vary, with EDGAR down-scaling national  
159 totals to finer scales using spatial information about the sources using global datasets while the  
160 GHGI gridded inventory reflects emission factors and activity data used in the EPA U.S.  
161 Greenhouse Gas Inventory. In contrast, NOAA FOG focuses specifically on fossil methane  
162 emissions and is a hybrid inventory that integrates atmospheric CH<sub>4</sub> and NO<sub>2</sub> observations with  
163 activity-based NO<sub>2</sub> metrics (Francoeur et al. 2021). While these inventories show considerable  
164 overlap in the location of emissions, differences can be large, even when aggregating from the  
165 original 0.1 degree grid of the inventories to the 1 degree grid shown for Figure 1.

166  
167 As stated previously, our goal for this study is to demonstrate a benchmark for U.S.  
168 methane emission gridded inventories and their changes from 2012 to 2020. These comparisons  
169 are documented through publicly accessible at Zenodo (Worden and Pandey 2025; Pandey and  
170 Worden 2025) (<https://doi.org/10.5281/zenodo.15786797>,  
171 <https://doi.org/10.5281/zenodo.16921536>); Jupyter notebooks are provided in the Pandey and  
172 Worden link that demonstrate how to compare gridded inventories to GOSAT-based emissions.  
173 These benchmarks will be updated as newer datasets, such as inverse analyses using Sentinel-5P  
174 TROPOMI (Tropospheric Ozone Monitoring Instrument) observations, become available (e.g.,  
175 Nesser et al. 2024; Hancock et al. 2025). Readers unfamiliar with the Bayesian attribution  
176 framework, the GOSAT inversion, or the specific inventories compared are encouraged to  
177 consult the appendices, where these methods are summarized, or our previously published work  
178 on the subject (Cusworth et al. 2021; Worden et al. 2022,2023).  
179



180 **2. Integrated total and sectoral USA emissions for 2015**

181

182 Table 1 summarizes U.S. methane emissions by sector for 2015, based on the GOSAT  
 183 data and the sectoral attribution approach described in this study (Appendix A). The error  
 184 characterization (Appendix B) includes uncertainties from the *a priori* as well as measurement  
 185 and model systematic error. The prior emissions are taken from Worden *et al.* (2023). Table 1  
 186 also shows a quantity called the Degrees of Freedom for Signal (DOFS), which is given by the  
 187 trace of the averaging-kernel matrix for the corresponding state-vector elements in  $\mathbf{z}$ . The DOFS  
 188 describe the extent to which the estimate is informed by observations rather than prior  
 189 assumptions (Appendix B), as well as the spatial information content. For example, from  
 190 Equation 2, if  $\mathbf{A} \approx \mathbf{0}$  (equivalent to DOFS = 0), observations say essentially nothing about the  
 191 emissions and the estimate reduces to the prior. If  $\mathbf{A}$  is the identity matrix, then the DOFS equals  
 192 the number of state-vector elements and the estimate exactly reflects the true distribution,  
 193 modified by the expected uncertainties (Appendix B). The DOFS reported in Table 1 refer to the  
 194 spatially distributed estimate, not for the total emissions value. Hence, DOFS > 1 means there is  
 195 at least some spatial information for that sector’s estimate.

196 For this GOSAT-based benchmark, the highest information content is available for total,  
 197 livestock, and oil and gas (O&G) emissions, while waste emissions estimates are only  
 198 moderately constrained by the data, and rice and coal emissions have limited observational  
 199 information. This variability in information content underscores the need for careful  
 200 interpretation of top-down estimates, particularly when examining spatial and sectoral patterns or  
 201 trends.

202

203 Table 1: GOSAT-Based CONUS Anthropogenic Emissions and Information Content by  
 204 Sector (2015)

Sector	Emissions (Tg CH <sub>4</sub> /yr)	<i>A priori</i> (Tg CH <sub>4</sub> /yr)	DOFS*
Total	29.4 ± 1.5	28.2±2.0	3.4
Livestock	10.3 ± 1.2	9.2 ± 1.4	1.8
Rice	0.4 ± 0.1	0.4±0.1	0.0



Waste	4.5 ± 0.6	5.6±0.8	0.6
Oil & Gas	11.1 ± 0.9	9.9±1.2	1.0
Coal	3.1 ± 0.3	3.1±0.3	0.1

205

206 **Table 2** compares these emissions to previous inversions using atmospheric data and  
 207 with the inventories (Appendix C) discussed in this paper. As can be seen in Table 2, our  
 208 atmospheric based emissions are generally consistent (within 1-2 sigma of the calculated  
 209 uncertainty) with other studies, even considering that each study has different priors, systematic  
 210 errors, and sensitivity of the data to the underlying emissions. These comparisons reveal that the  
 211 total emissions from the atmospheric-based inversions are typically larger than the activity-based  
 212 estimates with the livestock and oil&gas sectors responsible for most of the discrepancy.

213

214

215

216 **Table 2: Comparison of Methane Emissions by Study. All totals are CONUS**

217 anthropogenic; years as listed;

218 *(All values in Tg CH<sub>4</sub>/yr)*

Study	Total	Livestock	Rice	Waste	Oil & Gas	Coal
<b>(Atmospheric Inversions)</b>						
<b>GOSAT (2015 This Work)</b>	29.4 ± 1.5	10.4 ± 1.2	0.4 ± 0.1	4.6 ± 0.6	11.1 ± 0.9	3.1 ± 0.3
<b>GOSAT (2019)<sup>1</sup></b>	27.3 ± 3	9.9 ± 0.9	0.3 ± 0.1	4.0 ± 0.7	10.3 ± 1.0	2.8 ± 0.4
<b>TROPOMI (2019)<sup>2</sup></b>	30.9 ± 0.9	10.4 ± 0.3	N/A	6.9 ± 0.6	10.4 ± 0.3	1.5 ± 0.4
<b>GOSAT + Surface (2009– 2020)<sup>3</sup></b>	29.1 ± 0.5	8.8 ± 0.3	N/A	4.2 ± 0.1	14.1 ± 0.2	2 ± 0.4
<b>GOSAT (2010–2015)<sup>4</sup></b>	31 ± 1.0	9.4 ± 0.4	0.4 ± 0.2	6.2 ± 0.2	11.1 ± 0.6	3.2 ± 0.1
<b>In Situ (2007–2008)<sup>5</sup></b>	33.4 ± 2	N/A	N/A	N/A	N/A	N/A
<b>In Situ (2003)<sup>6</sup></b>	32.4 ± 5	N/A	N/A	N/A	N/A	N/A
<b>(Activity Models and Year)</b>						



<b>GHGI (2015)<sup>7</sup></b>	23.7±2.1	8.9±1.4	0.6±0.3	4.8±1.4	6.9±1	2.5±0.4
<b>EDGAR (2015)<sup>8</sup></b>	25.7±2.1	8.6±1.4	0.3±0.1	4.3±1.3	10.1±1	2.4±0.4
<b>NOAA FOG (2015)<sup>9</sup></b>					14.1 ± 2	

219

220 Table 2 lists emissions from several atmospheric-based inversions, excluding natural sources and  
 221 fire emissions, as well as from the gridded EPA GHGI, EDGAR 2024, and FOG inventories.

222 References: (1) Worden *et al.* 2022, (2) Nesser *et al.* 2024, (3) Janardanan *et al.* (2024), (4)  
 223 Maasackers *et al.* (2019), (5) Miller *et al.* (2013), (6) Kort *et al.* (2008), (7) Maasackers *et al.*  
 224 (2016, 2023), (8) Crippa *et al.* (2024), (9) Francoeur *et al.* (2021).

225

226

227 *2.1 Oil and Gas Emissions (GOSAT, FOG, EPA, and EDGAR)*

228

229 We next compare the GOSAT-based emissions for O&G to those from NOAA FOG,  
 230 GHGI, and EDGAR inventories. In particular, we demonstrate how applying the inversion  
 231 operator to these inventories modifies our interpretation of the comparison.

232

233 **Spatial Distribution for 2015:** Figures 2 through 4 compare the spatial distribution of U.S. oil  
 234 and gas (O&G) methane emissions in 2015 from the GOSAT inversion with those from the  
 235 FOG, GHGI, and EDGAR (2024 release, Crippa et al., 2024) inventories respectively. These  
 236 comparisons demonstrate the importance of accounting for the varying information content of  
 237 the GOSAT inversion, which is influenced by both the prior emissions used in the inversion and  
 238 the sensitivity of the aggregated satellite observations to underlying emission patterns (Worden  
 239 et al., 2023 and references therein). In Figure 2, the upper left panel (a) shows the GOSAT based  
 240 estimate. The upper right panel (b) shows the original FOG emissions. The middle left panel (c)  
 241 shows the difference between the top two. The middle right panel shows the difference between  
 242 FOG emissions and GOSAT based emissions after applying the inversion operator (denoted  
 243 AK). All figures use 1x1 degree gridding. The bottom right panel (E) shows the diagonal of the  
 244 averaging kernel (or DOFS) corresponding to that location for oil and gas emissions. As seen in  
 245 the left panel of Figure 2, significant regional discrepancies between the GOSAT and FOG  
 246 inventories exist, with similar magnitude differences as shown in Figure 1. However, after



247 applying the inversion operator (Equation 2) to the FOG inventory (labeled FOG AK), many of  
248 these differences are greatly reduced (middle right panel)

249 Small differences between GOSAT and the inventory, after applying the inversion operator, can  
250 also occur because of limited sensitivity, as indicated by the DOFS, for example over the Bakken  
251 region of North Dakota. As discussed previously and shown in Equation 2 and Appendix B, in  
252 such cases the difference between the GOSAT estimate and the inventory adjusted by the  
253 inversion operator should be close to zero, because both terms reduce to  $\sim Z_A$ . In contrast, the  
254 GOSAT estimate shows increased sensitivity to emissions in Oklahoma, Texas, and Louisiana.  
255 Based on this comparison, and on the integrated total emissions in the next section, we conclude  
256 that the GOSAT estimate does not falsify the spatial distribution of methane emissions posited  
257 by the FOG oil and gas inventory.

258

### 259 **Interpreting Comparisons between GOSAT, EDGAR, and GHGI emissions:**

260

261 Comparisons between GOSAT and EDGAR (Figure 3) and between GOSAT and EPA GHGI  
262 (Figure 4) show larger discrepancies, even after applying the inversion operator, particularly in  
263 northwest Colorado, Texas, Oklahoma, and Louisiana. These patterns indicate substantial  
264 inventory uncertainties in well-observed regions with intensive oil and gas activity. Some  
265 regions are sparsely observed by GOSAT, so their contributions may be important but their  
266 uncertainties cannot be reliably assessed with this benchmark. When measurement cost is a  
267 constraint, the discrepancy hotspots identified here are high-value targets for additional  
268 observations, with expanded coverage of under-sampled regions as resources allow.

269

270 Previous studies (e.g., Alvarez et al. 2018; Cusworth et al. 2022; Sherwin et al., 2024)  
271 have shown that a small number of high emitters (e.g., <2%; Sherwin et al., 2024), likely due to  
272 unplanned mechanical failures, contribute disproportionately to the fossil methane budget. These  
273 sources are likely underrepresented or missing from activity-based inventories. The agreement  
274 between FOG and GOSAT supports this conclusion, as the FOG inventory integrates  
275 atmospheric CH<sub>4</sub> with NO<sub>x</sub> observations and activity metrics; these regional CH<sub>4</sub> observations  
276 capture emissions under-represented in purely bottom-up approaches. If such super-emitters are



277 entirely responsible for the discrepancies between GOSAT and the EPA GHGI and EDGAR  
278 inventories, then comparisons between the GOSAT, EPA, EDGAR, and FOG O&G emissions in  
279 Table 2 suggest these sources are undercounted by  $\sim 7$  Tg CH<sub>4</sub>/yr of reported natural gas  
280 emissions, far exceeding previous estimates, as previously documented in other studies (e.g.,  
281 Alvarez et al. 2018; Cusworth et al. 2022; Sherwin et al., 2024; Zavala-Araiza et al. 2015).

282  
283

284 **Integrated totals for 2015:** Figure 5 compares integrated total oil and gas (O&G) emissions  
285 derived from GOSAT with those from the FOG, GHGI, and EDGAR inventories.

286 Before applying the inversion operator, total FOG emissions are estimated at  $14.1 \pm 2$  Tg CH<sub>4</sub>  
287 yr<sup>-1</sup>. We assumed the same prior covariance structure ( $\mathbf{Z}_A$ , Appendix B; Worden et al., 2022,  
288 2023) for FOG as for the GOSAT *a priori*. This yields a smaller total uncertainty (2 Tg CH<sub>4</sub> yr<sup>-1</sup>)  
289 than the  $\sim 2.8$  Tg CH<sub>4</sub> yr<sup>-1</sup> uncertainty for total FOG O&G emissions inferred from a Monte Carlo  
290 analysis of NO<sub>x</sub> activity data (Francoeur *et al.*, 2021). Using a different covariance structure that  
291 is consistent with the stated uncertainty in total emissions could therefore change conclusions  
292 about whether the GOSAT estimate falsifies the FOG inventory, and the inversion-operator  
293 methodology in Equation 2 would allow this. However, a full covariance is required, with  
294 explicitly computed off-diagonal terms such that, when projected to a single number, it  
295 reproduces the expected uncertainty reported in, for example, Francoeur et al. (2022).

296 After applying the inversion operator, the FOG total is reduced to 11.4 Tg CH<sub>4</sub> yr<sup>-1</sup>. The  
297 uncertainty shown for the modified FOG estimate (denoted FOG-AK) reflects the uncertainty in  
298 the difference between the GOSAT-based estimate and the FOG-AK estimate (Appendix B  
299 Equation 15), not the uncertainty of the FOG-AK estimate itself. Because the FOG-AK estimate  
300 is consistent with the GOSAT-based inversion within the reported uncertainty, this comparison  
301 suggests that the GOSAT estimate does not falsify the original, higher FOG total of 14.1 Tg CH<sub>4</sub>  
302 yr<sup>-1</sup>.



303 Figure 5 also shows comparisons to GHGI and EDGAR. For these inventories, uncertainties  
304 prior to applying the inversion operator are derived using the same prior covariance structure as  
305 for the GOSAT a priori, because published full covariances are not readily available.

306 In contrast to the FOG comparison, both the EPA and EDGAR estimates, with or without  
307 application of the inversion operator, are inconsistent with the GOSAT-based inversion. Their  
308 differences lie well outside the post-operator uncertainty shown for each inventory. As shown in  
309 Figures 3 and 4 these differences are spatially located primarily in the Texas, Oklahoma, and  
310 Louisiana regions. As noted previously, additional measurements here are therefore likely to  
311 reduce uncertainties in the USA O&G methane budget.

312

313 **Integrated Totals: 2012–2020:** Figure 6 shows annual methane emissions from 2012 to 2020.  
314 Despite substantial increases in oil and gas production over this period, all gridded inventories  
315 and the GOSAT top-down estimates show no significant change in total U.S. methane emissions,  
316 although the FOG inventory may have a slight increase. This apparent disconnect between rising  
317 production and stable emissions has been noted in several studies and is commonly attributed to  
318 improvements in production efficiency, leak detection, and emissions control technologies (e.g.,  
319 Lu et al., 2023). EPA GHGI supports this conclusion, showing relatively flat changes in fossil  
320 fuel methane emissions over the same period. This stability in the activity estimate is explained  
321 by offsetting trends, including a decline in exploration emissions due to fewer well completions,  
322 the adoption of lower-emitting equipment, and stable or slightly declining well counts  
323 (Maasakkers et al. 2023). For instance, while natural gas production increased by 26% and crude  
324 oil production by 67%, the number of active gas and oil wells remained roughly constant,  
325 declining slightly over the period. Emissions from gas systems were flat overall, with increases  
326 in gathering and boosting offset by decreases in production and processing. Similarly, petroleum  
327 system emissions rose by just 11% due to a significant drop in exploration-related emissions  
328 (Maasakkers et al. 2023).

329

330 *2.2 Livestock Emissions (GHGI and EDGAR)*

331



332 **Spatial Distribution for 2015:** Similar to Figures 2-4, Figures 7 and 8 show the spatial  
333 distribution of livestock methane emissions from GOSAT, EDGAR, and GHGI data. The FOG  
334 inventory is limited to oil and gas emissions and is therefore excluded from this and subsequent  
335 comparisons. Methane emissions from livestock generally scale with herd size, particularly dairy  
336 and beef cattle. Dairy cows typically emit more than twice as much methane as beef cows, due to  
337 higher enteric fermentation (Wolf et al., 2017; Hristov et al., 2017). Emissions vary  
338 geographically with management and environmental conditions (for example grazing  
339 practices, feed quality, and temperature, Wolf et al., 2017). Inventories account for this  
340 using region-specific emission factors, but if the factors used are not representative of  
341 actual local conditions, the resulting difference between the atmospheric based and activity  
342 based emissions should be spatially structured rather than random. Consistent with this,  
343 we observe systematic regional biases relative to the GOSAT-based estimates: inventories  
344 in California and the northern states are higher than GOSAT, whereas inventories in  
345 northern Texas are lower.

346

347 **Integrated Total for 2015:** Figure 9 compares integrated livestock methane emissions from  
348 GOSAT with GHGI and EDGAR inventories, each shown with and without the inversion  
349 operator applied. The GHGI and EDGAR totals differ modestly. The EPA total lies slightly  
350 outside the GOSAT uncertainty range, while the EDGAR total falls within it. However,  
351 agreement in totals does not imply agreement in spatial patterns. For EDGAR in particular,  
352 closer total agreement with GOSAT coincides with offsetting regional deviations, with positive  
353 differences in parts of the Midwest and negative differences in California. These cancellations  
354 reduce the apparent mismatch in the national total, which underscores the importance of  
355 evaluating spatial variability alongside integrated totals. Overall, comparisons of integrated  
356 totals and spatial patterns indicate substantial remaining uncertainty in livestock emissions.  
357 Additional measurements over California and the Midwest, especially in the Texas and  
358 Oklahoma region, would likely reduce this uncertainty.

359

360 **Integrated Totals for 2012-2020:** Figure 10 (and Table 2) shows comparisons between the  
361 integrated total livestock emissions from the GOSAT based inversion and the GHGI and  
362 EDGAR inventories. The GOSAT-based estimate as well as those from the GHGI and EDGAR



363 inventories do not observably change within the calculated uncertainties, except possibly for the  
364 year 2019. We therefore conclude that GOSAT based livestock emissions cannot falsify the  
365 posited (flat) trends from activity data (Maasakkers et al. 2021).

366

### 367 2.3 Waste (GHGI and EDGAR)

368 Figures 11 and 12 show the spatial distribution of methane emissions from the waste  
369 sector based on GOSAT, GHGI, and EDGAR estimates and Figure 13 shows the integrated total  
370 for 2015. The largest differences are for California for the EDGAR / GOSAT comparison. The  
371 integrated waste sector methane emissions from GOSAT are estimated at  $4.5 \pm 0.6$  Tg CH<sub>4</sub>/yr,  
372 while both GHGI and EDGAR report lower values of  $4.2 \pm 0.3$  Tg CH<sub>4</sub>/yr. These differences are  
373 not statistically significant, as the GOSAT estimate lies within the uncertainty range of both  
374 inventories (after applying the inversion operator). However, there is very limited spatial  
375 information content in the GOSAT waste estimate (~0.6 DOFS total). Consequently, the spatial  
376 differences shown in the right-bottom panel don't show meaningful differences between the  
377 inventories and the GOSAT waste estimate for most of the country.

378

## 379 3. Summary and Future Directions

380

381 Top-down methane emissions estimates vary in their information content depending on  
382 the emission sector and observing system. For these GOSAT based emissions estimates,  
383 information content is greatest for oil and gas and livestock, so these sectors are best suited for  
384 inventory evaluation using the results shown here. Waste, coal, and rice exhibit lower  
385 information content in this analysis because GOSAT does not adequately sample methane  
386 variability attributable to those sources. Even so, our information-content-based comparison  
387 identifies where additional measurements would yield the largest uncertainty reductions in  
388 gridded inventories.

389 In particular, our results highlight the need for targeted measurement campaigns,  
390 especially in the Texas, Oklahoma, and Louisiana drilling basins, where additional data can most  
391 effectively reduce inventory uncertainties. For the livestock sector, California and Northern  
392 Texas stands out as key regions where improved activity based and atmospheric methane



393 observation can have the highest impact. These findings underscore the importance of  
394 prioritizing high-emitting or uncertain regions to refine national methane budgets.  
395 Beyond regional targeting, improving inversion resolution is also key. Higher-resolution flux  
396 estimates, whether through satellites like TROPOMI or plume-resolving instruments (e.g., Jacob  
397 et al. 2022; Pandey et al. 2025 and refs therein), are particularly needed for sectors such as waste,  
398 coal, and oil and gas, where coarse-resolution inversions struggle to isolate source signals. In  
399 particular, integrating plume-resolving and area-flux estimates enhances the sectoral attribution  
400 of emissions and improves the information content for inventory evaluation (Pandey *et al.* 2025).

401

402       **(Trends)** Inversions conducted using GOSAT data and GEOS-Chem (see references in  
403 Table 2), show no discernible trend over the analysis period, which is consistent with all three  
404 gridded inventories discussed in this manuscript. However, the fact that other inversions show  
405 different trends highlights the importance of benchmarking approaches (Janardanan et al. 2024),  
406 not only for validating inventories but also for identifying uncertainties in inversion outputs  
407 themselves. These differences matter for informing effective remediation strategies and setting  
408 realistic expectations for emission reductions.

409       As satellite constellations improve in spatial resolution, sampling, and accuracy, top-  
410 down flux estimates become more accurate at higher spatial resolution (e.g., Jacob et al., 2022).  
411 Using TROPOMI, Nesser et al. (2024) produced a 2019 North American emissions map with a  
412 degree of freedom for signal (DOFS) of ~772, more than two orders of magnitude higher than in  
413 our GOSAT record, driven by a similar increase in observations. This resolution enables explicit  
414 estimation of many large sources, including landfills. East et al. (2025) extended this approach to  
415 global coverage at similar ~25 km gridding. Building a benchmark from the combined record  
416 will help evaluate how countries have managed emissions before and after the Global Methane  
417 Pledge, which targets a 30 percent reduction from 2020 to 2030. Our approach shows how  
418 inventories can be benchmarked against these improved flux estimates to reduce uncertainty,  
419 especially smoothing error, without re-running inversions with inventory priors. Combining  
420 high-resolution, independent datasets will support more accurate methane inventories, clarify  
421 source trends, and inform effective mitigation strategies.



## 422 **Appendices**

### 423 **Appendix A: GOSAT Methane Fluxes and Projection to USA Emissions by Sector**

424 **(Overview)** Yearly sectoral emissions by region based on the satellite data are generated in a two  
425 step process. The first step is to quantify global integrated fluxes using total atmospheric column  
426 methane data from the Japanese GOSAT (Greenhouse gases Observing SATellite) instrument  
427 (Parker *et al.* 2011) and the GEOS-Chem model (Zhang *et al.*, 2021). The approach used to  
428 generate fluxes has been extensively documented in past literature (e.g. Zhang *et al.*, 2021, Qu *et*  
429 *al.*, 2024), and we refer the reader to these articles. The state vector for this inversion include 1)  
430 yearly anthropogenic methane emissions between 2010 and 2022 at a gridding of 5x4 degrees  
431 (longitude/latitude) and we use the estimates between 2012 and 2020 for this study, 2) wetland  
432 methane emissions for specified regions for each month between 2010 to 2022), and 3) the  
433 yearly hemispheric methane sink. The second step (next section) is a linear estimate based on an  
434 optimal estimation sectoral emissions attribution approach (Cusworth *et al.* 2021; Worden *et al.*  
435 2022) that projects the integrated anthropogenic fluxes to emissions by sector and trends at the  
436 same 5x4 degree gridding and then again at 1x1 degree (lon/lat) gridding over the USA. This  
437 projection accounts for the prior distribution and uncertainties in the emissions (e.g. Worden *et*  
438 *al.* 2022). We next provide more detail on projection/attribution methodology as it is relevant to  
439 the benchmarking methodology that is the focus of this paper.

440 **(Sectoral attribution of fluxes to emissions)** We use a Bayesian based approach to project the  
441 fluxes described in the previous section (at 5x4 degrees lon/lat) to emissions by sector at 1x1  
442 degree. The full methodology is described in Cusworth *et al.* (2021) and first applied to methane  
443 fluxes in Worden *et al.* (2022) and again in Worden *et al.* (2023). This approach is equivalent to  
444 swapping the *a priori* assumptions, given by  $\mathbf{x}_A$  and  $\mathbf{S}_A$ , to a different state vector  $\mathbf{z}_A$  (and *a priori*  
445 covariance  $\mathbf{Z}_A$ ) when a linear relationship between the different state vectors  $\mathbf{x}$  and  $\mathbf{z}$  exist. The  
446 approach provides the full posterior and prior covariances and priors needed to account for the  
447 varying information content of satellite based emissions estimates when comparing these  
448 emissions to either each other (e.g. between years) or to inventories (Worden *et al.* 2023) or to  
449 other estimates. We refer the reader to these papers, starting with Cusworth *et al.* (2021) for the  
450 primary derivation, and summarize here.



451

452 Given a linear mapping between one state vector and another (e.g. between fluxes  $\mathbf{x}$  at 5x4  
453 degrees versus emissions  $\mathbf{z}$  at 5x4 degrees or alternatively emissions at 1x1 degree):

454

$$455 \quad \mathbf{x} = \mathbf{Mz}, \quad (4)$$

456

457 As discussed in Worden et al. (2023), the solution for projecting fluxes back to emissions takes  
458 the form:

459

$$460 \quad \hat{\mathbf{z}} = \mathbf{z}_A + \hat{\mathbf{Z}}\mathbf{M}^T\hat{\mathbf{S}}^{-1}[(\mathbf{I} - \hat{\mathbf{S}}\mathbf{S}_A^{-1})(\mathbf{x}_A - \mathbf{Mz}_A) + (\hat{\mathbf{x}} - \mathbf{x}_A)] \quad (5)$$

461

462 where the  $\hat{\mathbf{z}}$  and  $\mathbf{z}_A$  is the posterior and prior emissions state vector respectively with posterior  
463 and prior error covariance  $\hat{\mathbf{Z}}$ ,  $\mathbf{Z}_A$  respectively.

464

465 The posterior emission error covariance matrix  $\hat{\mathbf{Z}}$  is calculated explicitly given  $\mathbf{M}$ ,  $\mathbf{S}_A$ ,  $\hat{\mathbf{S}}$ , and  
466 prior emissions error covariance matrix  $\mathbf{Z}_A$ :

467

$$468 \quad \hat{\mathbf{Z}} = (\mathbf{M}^T(\hat{\mathbf{S}}^{-1} - \mathbf{S}_A^{-1})\mathbf{M} + \mathbf{Z}_A^{-1})^{-1} \quad (6)$$

469

470

471 Here, the  $\hat{\mathbf{S}}$  is the posterior covariance for the fluxes described in the Qu *et al.* (2024), with prior  
472 error covariance  $\mathbf{S}_A$ , given as a diagonal matrix with values of 0.5 (squared). The  $\mathbf{I}$  is the identity  
473 matrix. The prior covariances for each emission category (livestock, waste, rice, coal, oil and  
474 gas, and fires) are described in Worden et al. (2022) and Worden et al. (2023).

475

476

477 ***Uncertainty Calculation***

478



479 After projecting the estimate for integrated fluxes at 5x4 degrees ( $\hat{\mathbf{x}}$ ) to emissions by sector at  
480 1x1 degree ( $\hat{\mathbf{z}}$ ), we can describe  $\hat{\mathbf{z}}$  using Equation 2 with corresponding averaging kernel as  
481 discussed in the introduction (and now including uncertainties):

482

$$483 \quad \hat{\mathbf{z}} = \mathbf{z}_A + \mathbf{A}(\mathbf{z} - \mathbf{z}_A) + \boldsymbol{\delta}_n + \boldsymbol{\delta}_m \quad (7)$$

484

485 where  $\boldsymbol{\delta}_n$  and  $\boldsymbol{\delta}_m$  are the errors from measurement error and model error respectively. The  
486 measurement and model errors are discussed in Worden *et al.* (2022, 2023). The error  
487 covariance for  $\hat{\mathbf{z}}$  is then given by:

488

$$489 \quad E\|\hat{\mathbf{z}} - \mathbf{z}\|^2 = \mathbf{Z}_{\text{total}} = (\mathbf{I} - \mathbf{A})\mathbf{Z}_A(\mathbf{I} - \mathbf{A})^T + \mathbf{S}_n + \mathbf{S}_m \quad (8)$$

490

491 Note that the inverse of the Hessian (Equation 6) is equivalent to the first two terms (Worden *et al.*  
492 *et al.* 2004; Bowman *et al.* 2006):

493

$$494 \quad \hat{\mathbf{Z}} = (\mathbf{I} - \mathbf{A})\mathbf{Z}_A(\mathbf{I} - \mathbf{A})^T + \mathbf{S}_n \quad (9)$$

495

496 Equation 9 allows us to separate the “smoothing error” (the first term on the RHS of Equation 9),  
497 from the measurement error in order to better evaluate comparisons between the GOSAT and  
498 inventory methane estimates as discussed in the next section.

499

500 In order to calculate the emissions for either a region (e.g. USA) or a category of emissions (e.g.  
501 rice), we must first sum the corresponding elements of the state vector:

502

503

$$504 \quad \mathbf{z}_i = \mathbf{h}_i \hat{\mathbf{z}}, \quad (10)$$

505

506 Where  $\mathbf{h}_i$  is a column vector that projects the desired elements of  $\hat{\mathbf{z}}$  to region or sector  $i$ ,  $\mathbf{z}_i$ . As  
507 discussed in Worden *et al.* (2022), the uncertainty of  $\mathbf{z}_i$  is then given by

508

$$509 \quad \sigma_i^2 = \mathbf{h}_i \mathbf{Z}_{\text{total}} \mathbf{h}_i^T \quad (11)$$



510

511

512 As discussed in these previous papers, this uncertainty calculation accounts for the effects of  
513 cross-terms (e.g. wetlands, OH, fires). Equation (11) is what is used to calculate the  
514 uncertainties shown in the figures and the tables in this paper.

515

516 **Appendix B: Bayesian / Optimal Estimation Approach for Comparing Inventory to top-**  
517 **down Inversion**

518 To compare a  $0.1^\circ \times 0.1^\circ$  inventory with top-down fluxes based on an inversion of atmospheric  
519 data, we first project the inventory to the same spatial scale as the top-down fluxes and then  
520 account for the sensitivity of the top-down estimates. The native resolution of the gridded  
521 inventories is  $0.1^\circ$ , provided by sector. In contrast, the GOSAT based fluxes are at a coarser  
522 resolution of  $5^\circ \times 4^\circ$  (longitude  $\times$  latitude) and represent integrated fluxes (Qu et al., 2024) with  
523 no sectoral specificity in each grid. Our approach is to first re-grid the inventory to  $1^\circ \times 1^\circ$ , while  
524 retaining sectoral distinctions (e.g., livestock, waste, rice, coal, oil & gas). As discussed in the  
525 following paragraph, we then project the  $5^\circ \times 4^\circ$  GOSAT-inverted methane fluxes to sector-  
526 specific emissions at  $1^\circ \times 1^\circ$  resolution as discussed in Appendix A. We selected this  
527 intermediate resolution to better represent national emission patterns, as a  $5^\circ \times 4^\circ$  grid can cause  
528 significant overlapping flux contributions from neighboring countries such as the United States,  
529 Canada, and Mexico.

530

531 The comparison approach is described in Worden *et al.* (2023) and summarized here. We next  
532 project the inventory ( $z_i$ ) through the “inversion operator” (Equation 2) in order to account for  
533 the choice of a priori in the inversion and the sensitivity of the emissions (Rodgers 2000, Worden  
534 et al. 2022, 2023).

535

536  $\hat{z}_i = z_A + A(z_i - z_A)$  (12)

537



538 Where  $\mathbf{z}_A$  is a vector describing the *a priori* methane emissions used for the top-down estimate  
539 and  $\mathbf{A}$  is the averaging kernel matrix calculated for that inversion. The averaging kernel matrix is  
540 a function of the prior and posterior covariance,  $\hat{\mathbf{Z}}$  and  $\mathbf{Z}_A$ :

541

$$542 \quad \mathbf{A} = \mathbf{I} - \hat{\mathbf{Z}}\mathbf{Z}_A^{-1} \quad (13)$$

543

544 The DOFS shown in Table 1 are calculated by taking the sum of diagonal elements (or trace) of  
545 the averaging kernel corresponding to the sector.

546

547 After application of the inversion operator a comparison of these modified inventory emissions  
548 with the GOSAT- based emissions (Cusworth et al. 2021, Worden et al. 2023, Appendix A) is  
549 given by:

550

$$551 \quad \hat{\mathbf{z}} - \hat{\mathbf{z}}_i = \mathbf{A}(\boldsymbol{\delta}_i) + \boldsymbol{\delta}_n + \boldsymbol{\delta}_m \quad (14)$$

552

553 Where  $\boldsymbol{\delta}_i$  is the uncertainty in the inventory,  $\boldsymbol{\delta}_n$  is the uncertainty in the inversely estimated  
554 emissions due to noise in the atmospheric data, and  $\boldsymbol{\delta}_m$  is the uncertainty in the model used to  
555 project concentrations to emissions. The effect of the prior,  $\mathbf{z}_A$ , is also removed in this  
556 comparison described by Equation 14 so that the inventory can be compared to the satellite based  
557 emissions without this large effect of smoothing error on the comparison (see subsequent figures  
558 and supplemental). The error of the difference between satellite estimate and this adjusted  
559 inventory is then the expectation of the difference:

560

561

$$562 \quad E\|\hat{\mathbf{z}} - \hat{\mathbf{z}}_i\| = \mathbf{A}\mathbf{S}_i\mathbf{A}^T + \mathbf{S}_n + \mathbf{S}_m \quad (15)$$

563

564 Where  $\mathbf{S}_i$  is the covariance for the inventory uncertainties  $\boldsymbol{\delta}_i$ ,  $\mathbf{S}_n$  is the measurement error  
565 projected to emissions, and  $\mathbf{S}_m$  is the model error. Note that  $\mathbf{S}_n$  is directly calculated from the  
566 inversion (Worden et al. 2023). The final term in Equation 15, the model error, can be highly  
567 challenging to quantify. Previous studies have pointed towards the vertical mixing in models as  
568 being the largest source of model error; too much or too little methane (or other trace gas) at the



569 surface as a result of incorrect mixing leads to inaccurate surface flux calculations (e.g. Jiang et  
570 al. 2013; Schuh et al. 2019; Mcnorton et al. 2020). These studies show that this effect is largest  
571 in the tropics where there is significant convection with an uncertainty that is about the same size  
572 as the data uncertainty. On the other hand, the mid-latitudes likely have smaller uncertainties of  
573 this type because of smaller uncertainties related to vertical mixing. For the purpose of this study  
574 we assume the model error is the same magnitude as the observation error  $\mathbf{S}_n$ ; however continued  
575 advances are needed in both quantifying and mitigating this term, and how it affects the  
576 emissions estimates, in order to improve confidence in the comparisons between inventories and  
577 satellite data.

578 Note that if the GOSAT-based emissions are directly compared to the inventory without  
579 first passing the inventory through the inversion operator, then the uncertainties in the  
580 comparison are much larger and less meaningful as they include both the smoothing error of the  
581 data and the full uncertainty of the inventory:

$$583 \quad E\|\hat{\mathbf{z}} - \mathbf{z}_i\| = \mathbf{S}_i + \mathbf{S}_n + \mathbf{S}_m + (\mathbf{I}-\mathbf{A})\mathbf{S}_A(\mathbf{I}-\mathbf{A})^T \quad (16)$$

584  
585  
586 As a demonstration, we compare the GOSAT based emissions to the inventories both directly  
587 (uncertainties from Equation 16) and after applying the inversion operator (e.g. see Figures 2-4).

588  
589 **Use of Prior Swapping to evaluate emissions:** Equation 3 represents an alternative but  
590 equivalent approach for mitigating smoothing error when comparing atmospheric based  
591 emissions estimates to an inventory. After “swapping” the prior used for the GOSAT based  
592 emissions estimate with the inventory the new estimate has the following form:

$$594 \quad \hat{\mathbf{z}}_{\text{GOSAT\_New}} = \mathbf{z}_I + \mathbf{A}(\mathbf{z}_{\text{True}} - \mathbf{z}_I) + \delta_n + \delta_m \quad (17)$$

595  
596 In this instance we want to take the expectation of the difference of  $\hat{\mathbf{z}}_{\text{GOSAT\_New}}$  and  $\mathbf{z}_I$  as  
597 Equation (3) is equivalent to using  $\mathbf{z}_I$  as the *a priori* in the inversion described by Equation 1:

$$598 \quad \hat{\mathbf{z}}_{\text{GOSAT\_New}} - \mathbf{z}_I = \mathbf{A}(\mathbf{z}_{\text{True}} - \mathbf{z}_I) = \mathbf{A}(\delta_I) + \delta_n + \delta_m \quad (18)$$



600

601 Equation 18 is the same as Equation 14 which demonstrates that the covariances as described by  
602 Equation 15 (and hence uncertainties) are the same using prior swapping or an inversion operator  
603 approach.

604

605

## 606 **Appendix C: Description of Inventories**

607

608

609 **(EPA GHGI)** The U.S. Environmental Protection Agency's (EPA) Inventory of U.S.  
610 Greenhouse Gas Emissions and Sinks (GHGI) provides annual estimates of methane emissions  
611 from anthropogenic sources. The gridded inventory used here covers emissions from sectors  
612 such as agriculture, energy, waste, and coal for the years 2012 to 2018 (Maasakkers et al. 2023).

613 1. **Total Methane Emissions:** Gridded GHGI reports U.S. CONUS methane  
614 emissions in 2015 at **23.7 Tg** of CH<sub>4</sub>, which accounts for approximately **7% of global**  
615 **anthropogenic methane emissions.**

616 2. **Sectoral Breakdown:** The Gridded GHGI includes methane emissions of 26  
617 individual sectors. The largest sources are (see Table 2):

618 ○ **Livestock and Rice:** Emissions from enteric fermentation and manure  
619 management constitute a significant portion of methane emissions from this sector  
620 (8.8), with total agricultural emissions reaching **9.4 Tg** in 2018.

621 ○ **Oil and Gas:** Methane emissions from the oil and gas sectors, including  
622 production & exploration, refining, transmission & storage, processing, and  
623 distribution, account for approximately **6.9 Tg**.

624 ○ **Waste:** Emissions from municipal solid waste (MSW) landfills, industrial  
625 landfills, wastewater treatment, and composting contributed to about **4.8 Tg**.

626 ○ **Coal Mines:** Methane from coal mining, including both active and abandoned  
627 mines, contributed approximately **2.5 Tg**.



628           3.       **Methodology:** The GHGI combines activity data with emission factors to  
629           estimate methane emissions. The inventory uses data from sources such as the EPA’s  
630           Greenhouse Gas Reporting Program (GHGRP) and U.S. Department of Agriculture  
631           (USDA). The gridded GHGI uses facility-level data as well as proxy data for sources  
632           with limited spatial information. to spatially and temporally disaggregate emissions

633           4.       **Uncertainty and Adjustments:** The uncertainty in methane emissions is  
634           accounted for with confidence intervals provided in the GHGI report. Recent updates to  
635           the GHGI methodology include the inclusion of large well blowouts and emissions from  
636           abandoned oil and gas wells, which had not been considered in previous iterations. The  
637           inventory is continuously updated to reduce uncertainties and improve accuracy.

638           5.       **Comparisons with Atmospheric Data:** The Gridded GHGI serves as a critical  
639           input for atmospheric inversions and can be compared with top-down estimates from  
640           satellite-based data, such as those from GOSAT.

641

642   **(EDGAR 2024)** The Emissions Database for Global Atmospheric Research

643

644   The EDGAR series of inventories provides gridded (0.1x0.1 degree) emissions of the key  
645   anthropogenic emissions contributing to the global methane budget. We refer the reader to  
646   Crippa et al. (2020, 2024) for a description of this inventory. Emissions are generated by  
647   downscaling national totals by sector using spatial proxies and projected to the 0.1 x 0.1 grid. In  
648   order to improve the accuracy of comparisons between the EDGAR inventory and the GOSAT-  
649   based fluxes, we regrid their sub-categories to livestock, waste, coal, gas, oil, and rice (e.g. see  
650   Figure 1 for the EDGAR 2024 oil&gas emissions).

651

652   **(NOAA FOG)** The NOAA fuel-based oil and gas (FOG) inventory provides oil and gas  
653   emissions for the contiguous United States (CONUS) gridded at 4km x 4km and are then  
654   regridded to (0.1 x 0.1 degree) for this work (Francoeur et al. 2021). The NOAA FOG methane  
655   emissions inventory is generated through a hybrid approach that combines activity data with  
656   atmospheric measurements to provide a more comprehensive and accurate assessment of



657 methane emissions from the oil and gas sector. FOG combines combustion activity of drilling  
658 and production engines with fuel-based nitrogen oxides (NO<sub>x</sub>) emission factors from  
659 measurements and empirical models (Gorchov-Negron *et al.* 2018). The activity-based NO<sub>x</sub>  
660 emissions have been evaluated with airborne NOAA WP-3 measurements over a comprehensive  
661 number of US oil and gas basins during the Southeast Nexus Study  
662 (<https://csl.noaa.gov/projects/senex/>) and Shale Oil and Natural Gas Nexus Study  
663 (<https://csl.noaa.gov/projects/songnex/>), as well as with spaceborne observations (Dix *et al.*  
664 2020, 2022). Oil and gas methane emissions are then inferred by tracer-tracer ratios observed by  
665 the aircraft relative to NO<sub>x</sub> analyzed for each oil and gas basin measured (Francoeur *et al.* 2021).  
666 The hybrid approach in principle allows for a better representation of emissions compared to  
667 traditional activity-based inventories as the atmospheric data likely better captures the effect of  
668 **fugitive emissions** and other hard-to-measure sources that are often underrepresented in other  
669 activity based inventory methods. Additionally, atmospheric measurements help to address  
670 uncertainties by cross-referencing emission estimates with observed methane concentrations,  
671 thus improving the overall reliability of the inventory.

672 Key findings from the FOG inventory include:

- 673 1. **Methane Emissions:** The FOG inventory estimates total methane emissions from  
674 oil and natural gas production **at 14.1 ± 2.0 Tg CH<sub>4</sub>/yr for 2015.**
- 675 2. **Sectoral Breakdown:** The FOG inventory includes methane emissions from  
676 drilling, production, gathering, and processing activities. The contribution of methane  
677 emissions from the production and drilling phases is particularly significant, comprising  
678 about **60% of total methane emissions** during the oil and gas production process.
- 679 3. **Uncertainty and Evaluation:** The methane estimates from the FOG inventory  
680 are supported by aircraft-derived "top-down" emission measurements, which help  
681 validate the inventory's accuracy. Uncertainties are evaluated through a Monte-Carlo  
682 analysis of the NO<sub>x</sub> emissions and emissions factors (Francoeur *et al.* 2021)

683

684 **Code Availability**



685 The code for the sectoral attribution is available here (Worden and Pandey 2025):

686 <https://doi.org/10.5281/zenodo.15786798>].

687 A Python notebook demonstrating the benchmarking approach with the GOSAT inversion fluxes

688 is available at Pandey, S., & Worden, J. (2025). Evaluation of Methane Emissions Inventory

689 Using Satellite Flux Inversions Data set <https://doi.org/10.5281/zenodo.16921536> (Pandey and

690 Worden 2025)

691

### 692 **Data Availability**

693 GOSAT-based fluxes and emissions by sector are also available on Zenodo:

694 <https://zenodo.org/records/15786798>. (Worden and Pandey 2025)

695

### 696 **Author Contributions**

697 JW designed the study, performed sectoral attribution, and wrote the paper draft SP performed

698 the inventory comparison analysis, made the figures and supported the paper writing. HN, JDM,

699 and KB supported the analysis and paper writing. CH and CL supported the FOG analysis. DG

700 and LS supported interpretation of the inventories. DJ, LE, DV, JE, and ZQ produced the

701 GOSAT fluxes, supported the interpretation, and reviewed the paper.

702

703 **Competing Interests: The authors declare that to their knowledge there are no competing**  
704 **interests.**

705

### 706 **Acknowledgements**

707

708 Part of this research was carried out at the Jet Propulsion Laboratory, California Institute of

709 Technology, under a contract with the National Aeronautics and Space Administration. Chatgpt

710 used to support paper editing.

711

### 712 **Financial Support**

713

714 This work is funded by the NASA Carbon Monitoring System (Carbon Monitoring System

715 NNH23ZDA001N-CMS) and through the NASA Greenhouse Gas Center.



716 **References**

717

718 Alvarez, R. A., Zavala-Araiza, D., Lyon, D. R., Allen, D. T., Barkley, Z. R., Brandt, A. R., et al.  
719 (2018). Assessment of methane emissions from the U.S. oil and gas supply chain. *Science*,  
720 361(6398), eaar7204. <https://doi.org/10.1126/science.aar7204>

721 Barkley, Z. R., Lauvaux, T., Davis, K. J., Miles, N. L., Richardson, S. J., Jacobson, G., et al.  
722 (2022). Estimating methane emissions from the Marcellus and Delaware Basins using continuous  
723 tower observations. *Atmospheric Chemistry and Physics*, 23, 6127–6145.  
724 <https://doi.org/10.5194/acp-23-6127-2023>

725 Bowman, K. W., Rodgers, C. D., Kulawik, S. S., Worden, J., Sarkissian, E., Osterman, G., Steck,  
726 T., Lou, M., Eldering, A., Shephard, M., Worden, H., Lampel, M., Clough, S., Brown, P.,  
727 Rinsland, C., Gunson, M., and Beer, R.: Tropospheric Emission Spectrometer: Retrieval Method  
728 and Error Analysis, *Ieee T Geosci Remote*, 44, 1297–1307,  
729 <https://doi.org/10.1109/tgrs.2006.871234>, 2006.

730 Crippa, M., Solazzo, E., Huang, G., Guizzardi, D., Koffi, E., Muntean, M., et al. (2020). High  
731 resolution temporal profiles in the Emissions Database for Global Atmospheric Research.  
732 *Scientific Data*, 7, 121. <https://doi.org/10.1038/s41597-020-0462-2>

733 Crippa, M., Guizzardi, D., Pagani, F., Schiavina, M., Melchiorri, M., Pisoni, E., et al. (2024).  
734 Insights into the spatial distribution of global, national, and subnational greenhouse gas  
735 emissions in the Emissions Database for Global Atmospheric Research (EDGAR v8.0). *Earth*  
736 *System Science Data*, 16(6), 2811–2830. <https://doi.org/10.5194/essd-16-2811-2024>

737 Crippa, M., Guizzardi, D., Pagani, F., Banja, M., Muntean, M., Schaaf, E., Monforti-Ferrario, F.,  
738 Becker, W., Quadrelli, R., Riskey Martin, A., Taghavi-Moharamli, P., Köykkä, J., Grassi, G.,  
739 Rossi, S., Melo, J., Oom, D., Branco, A., San-Miguel, J., Manca, G., Pisoni, E., Vignati, E. and  
740 Pekar, F., GHG emissions of all world countries, Publications Office of the European Union,  
741 Luxembourg, 2024, doi:10.2760/4002897, JRC138862

742



- 743 Cusworth, D. H., Bloom, A. A., Ma, S., Miller, C. E., Bowman, K., Yin, Y., et al. (2021). A  
744 Bayesian framework for deriving sector-based methane emissions from top-down fluxes.  
745 *Communications Earth & Environment*, 2, 242. <https://doi.org/10.1038/s43247-021-00312-6>
- 746 Cusworth, D. H., Duren, R. M., Ayasse, A. K., Jiorle, R., Howell, K., Aubrey, A., et al. (2024).  
747 Quantifying methane emissions from United States landfills. *Science*, 383(6690), 1499–1504.  
748 <https://doi.org/10.1126/science.adi7735>
- 749 Cusworth, D. H., Duren, R. M., Thorpe, A. K., Tseng, E., Thompson, D., Guha, A., et al. (2020).  
750 Using remote sensing to detect, validate, and quantify methane emissions from California solid  
751 waste operations. *Environmental Research Letters*, 15, 054012. <https://doi.org/10.1088/1748-9326/ab7b99>
- 753 Cusworth, D. H., Thorpe, A. K., Ayasse, A. K., Stepp, D., Heckler, J., Asner, G. P., et al. (2022).  
754 Strong methane point sources contribute a disproportionate fraction of total emissions across  
755 multiple basins in the United States. *Proceedings of the National Academy of Sciences*, 119,  
756 e2202338119. <https://doi.org/10.1073/pnas.2202338119>
- 757
- 758 Dix, B., Francoeur, C., Li, M., Serrano-Calvo, R., Levelt, P. F., Veeffkind, J. P., McDonald, B.  
759 C., and de Gouw, J. A.: Quantifying NO<sub>x</sub> emissions from U.S. oil and gas production regions  
760 using TROPOMI NO<sub>2</sub>, *ACS Earth Space Chem.*, 6(2), 403-414,  
761 <https://doi.org/10.1021/acsearthspacechem.1c00387>, 2022.
- 762
- 763 Dix, B., Bruin, J., Roosenbrand, E., Vlemmix, T., Francoeur, C., Gorchov-Negron, A. M.,  
764 McDonald, B., Zhizhin, M., Elvidge, C., Veeffkind, P., Levelt, P., and de Gouw, J. A.: Nitrogen  
765 oxide emissions from U.S. oil and gas production: Recent trends and source  
766 attribution, *Geophys. Res. Lett.*, 47(1), e2019GL085866, <https://doi.org/10.1029/2019GL085866>,  
767 2020.
- 768
- 769 East, J. D., Jacob, D. J., Jervis, D., Balasus, N., Estrada, L. A., Hancock, S. E., Sulprizio, M. P.,  
770 Thomas, J., Wang, X., Chen, Z., Varon, D. J., and Worden, J. R.: Worldwide inference of



771 national methane emissions by inversion of satellite observations with UNFCCC prior estimates,  
772 Nat. Commun., 16, 11004, <https://doi.org/10.1038/s41467-025-67122-8>, 2025.

773 [EDGAR \(Emissions Database for Global Atmospheric Research\) Community GHG Database, a](#)  
774 [collaboration between the European Commission, Joint Research Centre \(JRC\), the International](#)  
775 [Energy Agency \(IEA\), and comprising IEA-EDGAR CO<sub>2</sub>, EDGAR CH<sub>4</sub>, EDGAR N<sub>2</sub>O,](#)  
776 [EDGAR F-GASES version 2024 European Commission, JRC \(Datasets\).](#)  
777 [https://edgar.jrc.ec.europa.eu/dataset\\_ghg2024](https://edgar.jrc.ec.europa.eu/dataset_ghg2024) (accessed: 1 October 2025)

778

779 [EPA \(U.S. Environmental Protection Agency\). \(2011\). Fact Sheet on Mandatory Reporting of](#)  
780 [Greenhouse Gases \(40 CFR part 98\). \[https://www.epa.gov/sites/default/files/2015-\]\(https://www.epa.gov/sites/default/files/2015-07/documents/part98factsheet.pdf\)](#)  
781 [07/documents/part98factsheet.pdf](#)

782 Etiope, G., Ciotoli, G., Schwietzke, S., & Schoell, M. (2018). Gridded maps of geological  
783 methane emissions and their isotopic signature. *Earth System Science Data*, 11, 1–22.  
784 <https://doi.org/10.5194/essd-11-1-2019>

785 Francoeur, C. B., McDonald, B. C., Gilman, J. B., Zarzana, K. J., Dix, B., Brown, S. S., et al.  
786 (2021). Quantifying methane and ozone precursor emissions from oil and gas production regions  
787 across the contiguous US. *Environmental Science & Technology*, 55(13), 9129–9139.  
788 <https://doi.org/10.1021/acs.est.0c07352>

789 Gorchov Negron, A. M., McDonald, B. C., McKeen, S. A., Peischl, J., Ahmadov, R., de Gouw,  
790 J. A., Frost, G. J., Hastings, M. G., Pollack, I. B., Ryerson, T. B., Thompson, C., Warneke, C.,  
791 and Trainer, M.: Development of a fuel-based oil and gas inventory of nitrogen oxides  
792 emissions, *Environ. Sci. Technol.*, **52**, 10175–10185, <https://doi.org/10.1021/acs.est.8b02245>,  
793 2018.

794 [Gordon, D. No Standard Oil: Managing Abundant Petroleum in a Warming World \(paperback](#)  
795 [edition\). Oxford University Press, 2025. \[https://global.oup.com/academic/product/no-standard-\]\(https://global.oup.com/academic/product/no-standard-oil-9780197832165?cc=us&lang=en&\)](#)  
796 [oil-9780197832165?cc=us&lang=en&](#)



- 797 Hancock, S. E., Jacob, D., Chen, Z., Nesser, H., Davitt, A., Varon, D. J., et al. (2025). Satellite  
798 quantification of methane emissions from South American countries: A high-resolution inversion  
799 of TROPOMI and GOSAT observations. *Atmospheric Chemistry and Physics*, 25, 797–833.  
800 <https://doi.org/10.5194/acp-25-797-2025>
- 801 Herman, R. L., Cherry, J. E., Young, J., Welker, J. M., Noone, D., Kulawik, S. S., & Worden, J.  
802 (2014). Aircraft validation of Aura Tropospheric Emission Spectrometer retrievals of HDO /  
803 H<sub>2</sub>O. *Atmospheric Measurement Techniques*, 120(9), 3127–3138. [https://doi.org/10.5194/amt-7-](https://doi.org/10.5194/amt-7-3127-2014)  
804 [3127-2014](https://doi.org/10.5194/amt-7-3127-2014)  
805
- 806 Hmiel, B., Petrenko, V. V., Dyonisius, M. N., Buizert, C., Smith, A. M., Place, P. F., et al.  
807 (2020). Preindustrial 14CH<sub>4</sub> indicates greater anthropogenic fossil CH<sub>4</sub> emissions. *Nature*, 578,  
808 409–412. <https://doi.org/10.1038/s41586-020-1991-8>
- 809 Hristov, A. N., Harper, M., Meinen, R., Day, R., Lopes, J., Ott, T., et al. (2017). Discrepancies  
810 and uncertainties in bottom-up gridded inventories of livestock methane emissions for the  
811 contiguous United States. *Environmental Science & Technology*, 51(23), 13668–13677.  
812 <https://doi.org/10.1021/acs.est.7b03332>
- 813 [IEA \(International Energy Agency\). \(2025\). Global Methane Tracker 2025.](https://www.iea.org/reports/global-methane-tracker-2025/key-findings)  
814 <https://www.iea.org/reports/global-methane-tracker-2025/key-findings>
- 815 Jacob, D. J., Varon, D. J., Cusworth, D. H., Dennison, P. E., Frankenberg, C., Gautam, R., et al.  
816 (2022). Quantifying methane emissions from the global scale down to point sources using  
817 satellite observations of atmospheric methane. *Atmospheric Chemistry and Physics*, 22, 9617–  
818 9646. <https://doi.org/10.5194/acp-22-9617-2022>
- 819 Janardanan, R., Maksyutov, S., Wang, F., Nayagam, L., Sahu, S. K., Mangaraj, P., et al. (2024).  
820 Country-level methane emissions and their sectoral trends during 2009–2020 estimated by high-  
821 resolution inversion of GOSAT and surface observations. *Environmental Research Letters*, 19,  
822 034007. <https://doi.org/10.1088/1748-9326/ad2436>



- 823 Kruskamp, N., Lohman, H., Burnette, A., Coxen, C., Ellermeier, N., Bollenbacher, J., Powers, J.,  
824 Coffield, S., Farhat, Y., and Maasakkers, J.: *Gridded U.S. Anthropogenic Methane Greenhouse*  
825 *Gas Inventory (gridded GHGI)*, Zenodo, <https://doi.org/10.5281/zenodo.16782735>, 2025.
- 826 Kort, E. A., Eluszkiewicz, J., Stephens, B. B., Miller, J. B., Gerbig, C., Nehrkorn, T., et al.  
827 (2008). Emissions of CH<sub>4</sub> and N<sub>2</sub>O over the United States and Canada based on a receptor-  
828 oriented modeling framework and COBRA-NA atmospheric observations. *Geophysical*  
829 *Research Letters*, 35, L18808. <https://doi.org/10.1029/2008GL034031>
- 830 Lu, X., Jacob, D. J., Zhang, Y., Shen, L., Sulprizio, M. P., Maasakkers, J. D., et al. (2023).  
831 Observation-derived 2010–2019 trends in methane emissions and intensities from U.S. oil and  
832 gas fields tied to activity metrics. *Proceedings of the National Academy of Sciences*, 120,  
833 e2217900120. <https://doi.org/10.1073/pnas.2217900120>
- 834 Maasakkers, J. D., Jacob, D. J., Sulprizio, M. P., Scarpelli, T. R., Nesser, H., Sheng, J., et al.  
835 (2021). 2010–2015 North American methane emissions, sectoral contributions, and trends: a  
836 high-resolution inversion of GOSAT observations of atmospheric methane. *Atmospheric*  
837 *Chemistry and Physics*, 21, 4339–4356. <https://doi.org/10.5194/acp-21-4339-2021>
- 838 Maasakkers, J. D., McDuffie, E. E., Sulprizio, M. P., Chen, C., Schultz, M., Brunelle, L., et al.  
839 (2023). A gridded inventory of annual 2012–2018 U.S. anthropogenic methane emissions.  
840 *Environmental Science & Technology*, 57(43), 16276–16288.  
841 <https://doi.org/10.1021/acs.est.3c05138>
- 842 Miller, S. M., Wofsy, S. C., Michalak, A. M., Kort, E. A., Andrews, A. E., Biraud, S. C., et al.  
843 (2013). Anthropogenic emissions of methane in the United States. *Proceedings of the National*  
844 *Academy of Sciences*, 110(50), 20018–20022. <https://doi.org/10.1073/pnas.1314392110>
- 845 Nesser, H., Jacob, D. J., Maasakkers, J. D., Lorente, A., Chen, Z., Lu, X., et al. (2024). High-  
846 resolution U.S. methane emissions inferred from an inversion of 2019 TROPOMI satellite data:  
847 Contributions from individual states, urban areas, and landfills. *Atmospheric Chemistry and*  
848 *Physics*, 24, 5069–5091. <https://doi.org/10.5194/acp-24-5069-2024>



- 849 Nisbet, E. G., Manning, M. R., Dlugokencky, E. J., Fisher, R. E., Lowry, D., Michel, S. E., et al.  
850 (2019). Very strong atmospheric methane growth in the 4 years 2014–2017: Implications for the  
851 Paris Agreement. *Global Biogeochemical Cycles*, 33, 318–342.  
852 <https://doi.org/10.1029/2018GB006009>
- 853 Pandey, S., Worden, J., Cusworth, D. H., Varon, D. J., Thill, M. D., Jacob, D. J., and Bowman,  
854 K. W.: Relating multi-scale plume detection and area estimates of methane emissions: a  
855 theoretical and empirical analysis, *Environ. Sci. Technol.*, 59, 7931–7947,  
856 <https://doi.org/10.1021/acs.est.4c07415>, 2025.
- 857 Pandey, S. and Worden, J.: *Evaluation of Methane Emissions Inventory Using Satellite Flux*  
858 *Inversions* (data set), Zenodo, <https://doi.org/10.5281/zenodo.16921536>, 2025.
- 859 Parker, R., Boesch, H., Cogan, A., Fraser, A., Feng, L., Palmer, P. I., et al. (2011). Methane  
860 observations from the Greenhouse Gases Observing SATellite: Comparison to ground-based  
861 TCCON data and model calculations. *Geophysical Research Letters*, 38, L15807.  
862 <https://doi.org/10.1029/2011GL047871>
- 863 Petrescu, A. M. R., Peters, G. P., Engelen, R., Houweling, S., Brunner, D., Tsuruta, A., et al.  
864 (2024). Comparison of observation- and inventory-based methane emissions for eight large  
865 global emitters. *Earth System Science Data*, 16, 4325–4350. [https://doi.org/10.5194/essd-16-](https://doi.org/10.5194/essd-16-4325-2024)  
866 [4325-2024](https://doi.org/10.5194/essd-16-4325-2024)
- 867 Qu, Z., Jacob, D. J., Zhang, Y., Shen, L., Varon, D. J., Lu, X., Scarpelli, T., Bloom, A., Worden,  
868 J., and Parker, R. J.: Attribution of the 2020 surge in atmospheric methane by inverse analysis of  
869 GOSAT observations, *Environ Res Lett*, <https://doi.org/10.1088/1748-9326/ac8754>, 2022.
- 870 Qu, Z., Jacob, D. J., Bloom, A. A., Worden, J. R., Parker, R. J., & Boesch, H. (2024). Inverse  
871 modeling of 2010–2022 satellite observations shows that inundation of the wet tropics drove the  
872 2020–2022 methane surge. *Proceedings of the National Academy of Sciences*, 121,  
873 e2402730121. <https://doi.org/10.1073/pnas.2402730121>



- 874 Rodgers, C. D., & Connor, B. J. (2003). Intercomparison of remote sounding instruments.  
875 *Journal of Geophysical Research: Atmospheres*, 108, 4116.  
876 <https://doi.org/10.1029/2002JD002299>
- 877 Saunio, M., Stavert, A. R., Poulter, B., Bousquet, P., Canadell, J. G., Jackson, R. B., et al.  
878 (2020). The global methane budget 2000–2017. *Earth System Science Data*, 12, 1561–1623.  
879 <https://doi.org/10.5194/essd-12-1561-2020>
- 880 Sherwin, E. D., Rutherford, J. S., Zhang, Z., Chen, Y., Wetherley, E. B., Yakovlev, P. V., et al.  
881 (2024). U.S. oil and gas system emissions from nearly one million aerial site measurements.  
882 *Nature*, 627, 328–334. <https://doi.org/10.1038/s41586-024-07117-5>
- 883 United States Environmental Protection Agency (EPA). (2023). Inventory of U.S. greenhouse  
884 gas emissions and sinks: 1990–2021 (EPA 430-R-23-002). Retrieved from  
885 <https://www.epa.gov/ghgemissions/inventory-us-greenhouse-gas-emissions-and-sinks>
- 886 Wecht, K. J., Jacob, D. J., & Sulprizio, M. P. (2014). Spatially resolving methane emissions in  
887 California: constraints from the CalNex aircraft campaign and from present (GOSAT, TES) and  
888 future (TROPOMI, .... *Atmospheric Chemistry and Physics*, 14(15). [https://doi.org/10.5194/acp-](https://doi.org/10.5194/acp-14-8173-2014)  
889 14-8173-2014  
890
- 891 Wolf, J., Asrar, G. R., & West, T. O. (2017). Revised methane emissions factors and spatially  
892 distributed annual carbon fluxes for global livestock. *Carbon Balance and Management*, 12, 16.  
893 <https://doi.org/10.1186/s13021-017-0084-y>
- 894 Worden, J., Kulawik, S., Shepard, M., Clough, S., Worden, H., Bowman, K., and Goldman, A.:  
895 Predicted errors of tropospheric emission spectrometer nadir retrievals from spectral window  
896 selection, *J Geophys Res Atmospheres* 1984 2012, 109, D09308,  
897 <https://doi.org/10.1029/2004jd004522>, 2004.  
898
- 899 Worden, J. R., Cusworth, D. H., Qu, Z., Yin, Y., Zhang, Y., Bloom, A. A., et al. (2022). The  
900 2019 methane budget and uncertainties at 1° resolution and each country through Bayesian



- 901 integration of GOSAT total column methane data and a priori inventory estimates. *Atmospheric*  
902 *Chemistry and Physics*, 22, 6811–6841. <https://doi.org/10.5194/acp-22-6811-2022>
- 903 Worden, J. R., Pandey, S., Zhang, Y., Cusworth, D. H., Qu, Z., Bloom, A. A., et al. (2023).  
904 Verifying methane inventories and trends with atmospheric methane data. *AGU Advances*, 4.  
905 <https://doi.org/10.1029/2023AV000871>
- 906 Worden, J. R. and Pandey, S.: *Evaluation of Methane Emissions Inventory Using Satellite Flux*  
907 *Inversions*, Zenodo, <https://doi.org/10.5281/zenodo.15786798>, 2025.
- 908 [World Bank. \(2025\). Global Gas Flaring Tracker Report.](#)  
909 [https://thedocs.worldbank.org/en/doc/bd2432bbb0e514986f382f61b14b2608-](https://thedocs.worldbank.org/en/doc/bd2432bbb0e514986f382f61b14b2608-0400072025/original/Global-Gas-Flaring-Tracker-Report-July-2025.pdf)  
910 [0400072025/original/Global-Gas-Flaring-Tracker-Report-July-2025.pdf](https://thedocs.worldbank.org/en/doc/bd2432bbb0e514986f382f61b14b2608-0400072025/original/Global-Gas-Flaring-Tracker-Report-July-2025.pdf)
- 911 Zavala-Araiza, D., Lyon, D. R., Alvarez, R. A., Davis, K. J., Harriss, R., Herndon, S. C., et al.  
912 (2015). Reconciling divergent estimates of oil and gas methane emissions. *Proceedings of the*  
913 *National Academy of Sciences*, 112, 15597–15602. <https://doi.org/10.1073/pnas.1522126112>
- 914 Zhang, Y., Jacob, D. J., Lu, X., Maasackers, J. D., Scarpelli, T. R., Sheng, J.-X., et al. (2021).  
915 Attribution of the accelerating increase in atmospheric methane during 2010–2018 by inverse  
916 analysis of GOSAT observations. *Atmospheric Chemistry and Physics*, 21, 3643–3666.  
917 <https://doi.org/10.5194/acp-21-3643-2021>
- 918 Zhang, P., Zhang, Y., and Liang, R.: 2025: Correction of simulation biases in stratospheric  
919 methane concentrations for the inverse analysis of satellite column observations, *J. Geophys.*  
920 *Res.-Atmos.*, 30, <https://doi.org/10.1029/2024JD042596>.

921

922



923 [Figure Captions](#)

924

925 Figure 1: (Top Panels) Mean Emissions for Oil and Gas for 2015 (at 1x1 degree lon/lat gridding)  
926 as calculated from the EPA, FOG, EDGAR inventories. (Bottom Panels) Differences between  
927 FOG and EPA and EDGAR and EPA.

928

929 Figure 2: Comparison of the U.S. oil and gas (O&G) methane emissions in 2015 from the  
930 GOSAT inversion with those from the FOG inventory. The upper left panel (a) shows the  
931 GOSAT based estimate. The upper right panel (b) shows the original FOG emissions. The  
932 middle left panel (c) shows the difference between the top two. The middle right panel shows the  
933 difference between FOG emissions and GOSAT based emissions after applying the inversion  
934 operator (denoted AK). All figures use 1x1 degree gridding; only differences larger than the  
935 corresponding calculated uncertainty are shown. The bottom right panel (E) shows the diagonal  
936 of the averaging kernel (or DOFS) corresponding to that location for oil and gas emissions.

937

938 Figure 3: Same as in Figure 2 but for the EDGAR inventory.

939

940 Figure 4: Same as in Figure 3 but for the EPA GHGI inventory.

941

942 **Figure 5:** Comparison of the integrated total oil and gas (O&G) emissions derived from GOSAT  
943 with those from the FOG, EPA GHGI , and EDGAR 2024 inventories, both with and without the  
944 inversion operator (AK) applied. Comparisons should be made between the GOSAT estimate  
945 and the inventories with inversion operator (AK) applied.

946

947 **Figure 6:** Integrated totals for oil and gas emissions between 2012 and 2020. The GOSAT  
948 inversion operator has been applied to the FOG, EPA GHGI , and EDGAR 2024 inventories; the  
949 biases between the comparisons are therefore not due to the prior used with the GOSAT  
950 inversion.

951 **Figure 7:** Similar to Figure 2 but for EDGAR 2024 livestock emissions



952

953 **Figure 8:** Similar to Figure 7 but for EPA GHGI livestock emissions

954

955 **Figure 9:** Comparison of the integrated livestock emissions derived from GOSAT with those  
956 from the EPA GHGI and EDGAR 2024 inventories, both with and without the inversion  
957 operator (AK) applied. Comparisons should be made between the GOSAT estimate and the  
958 inventories with inversion operator (AK) applied.

959

960 **Figure 10:** Integrated totals for Livestock Emissions between 2012 and 2020. The inversion  
961 operator has been applied to the inventories.

962

963 **Figure 11:** Similar to Figure 2 but for EDGAR 2024 waste emissions

964

965 **Figure 12:** Similar to Figure 3 but for EPA GHGI waste emissions

966

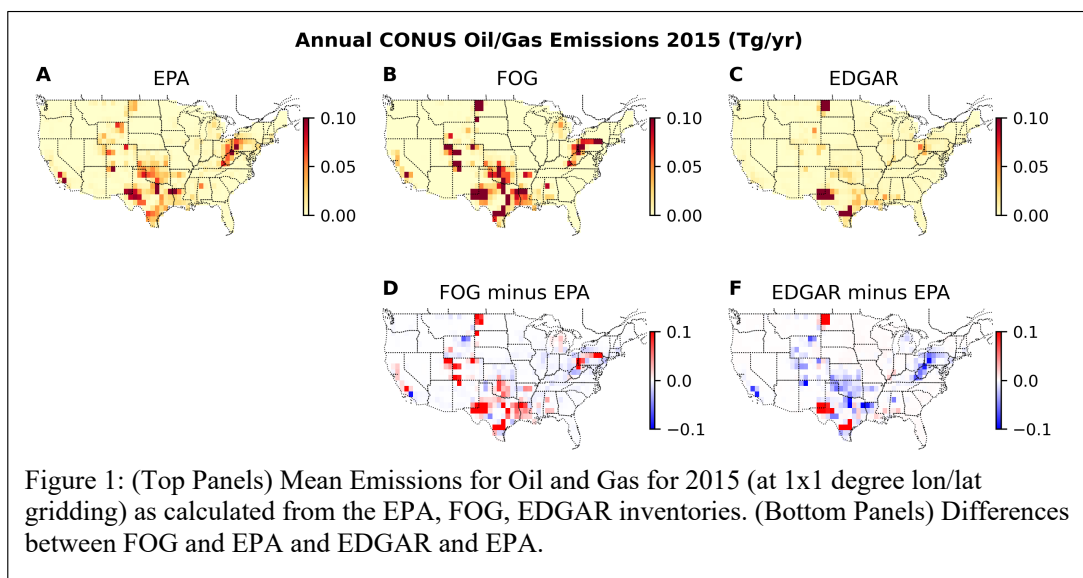
967 **Figure 13:** Integrated total methane emissions from the waste sector based on GOSAT, along  
968 with estimates from the EPA GHGI and EDGAR 2024 inventories, both with and without the  
969 inversion operator applied.

970



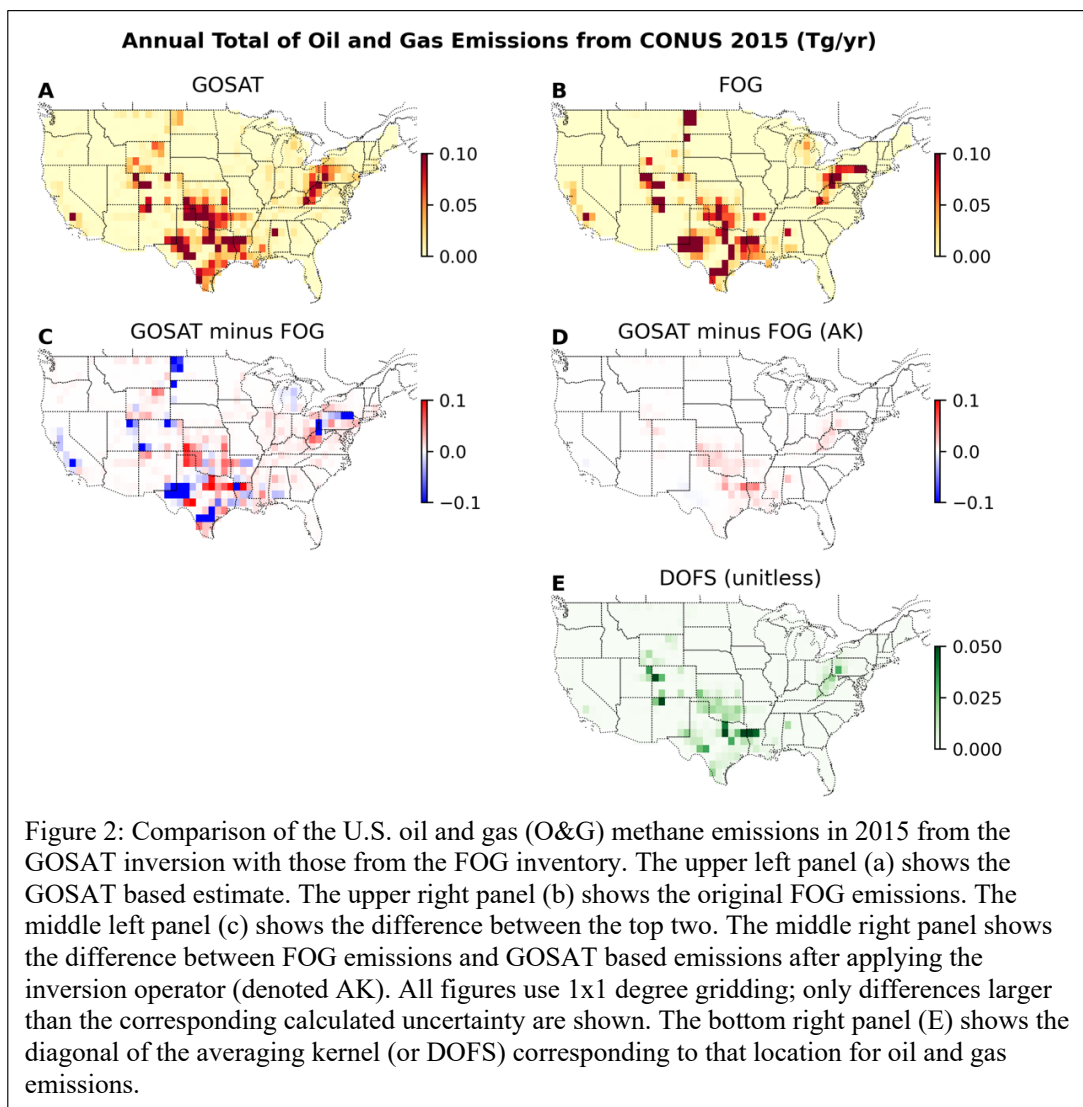
971 [Figures](#)

972



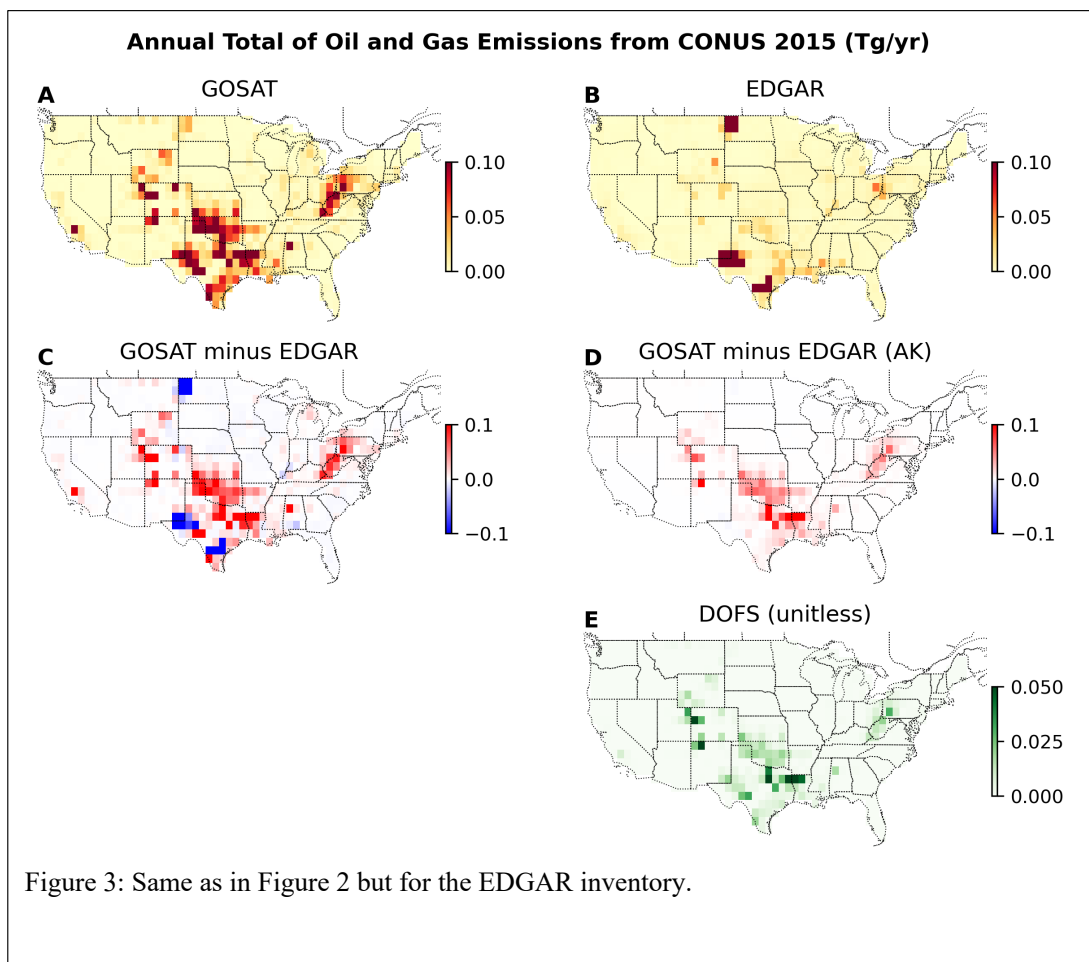


973



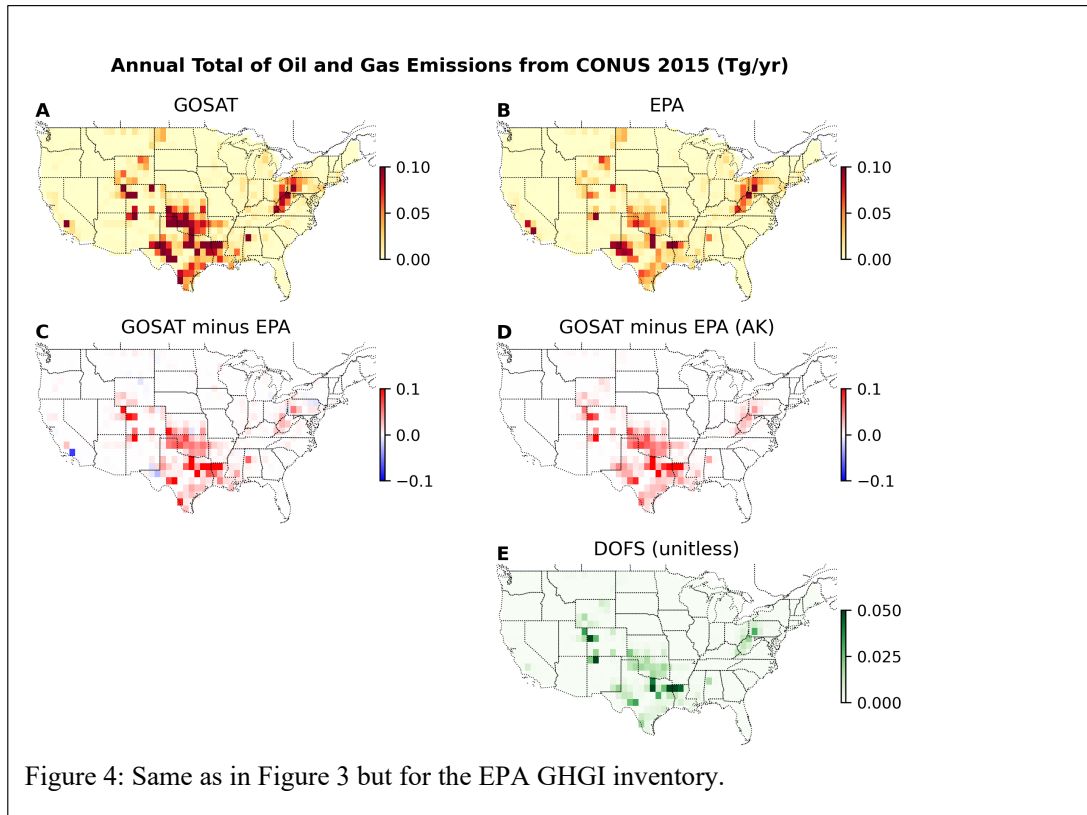


974



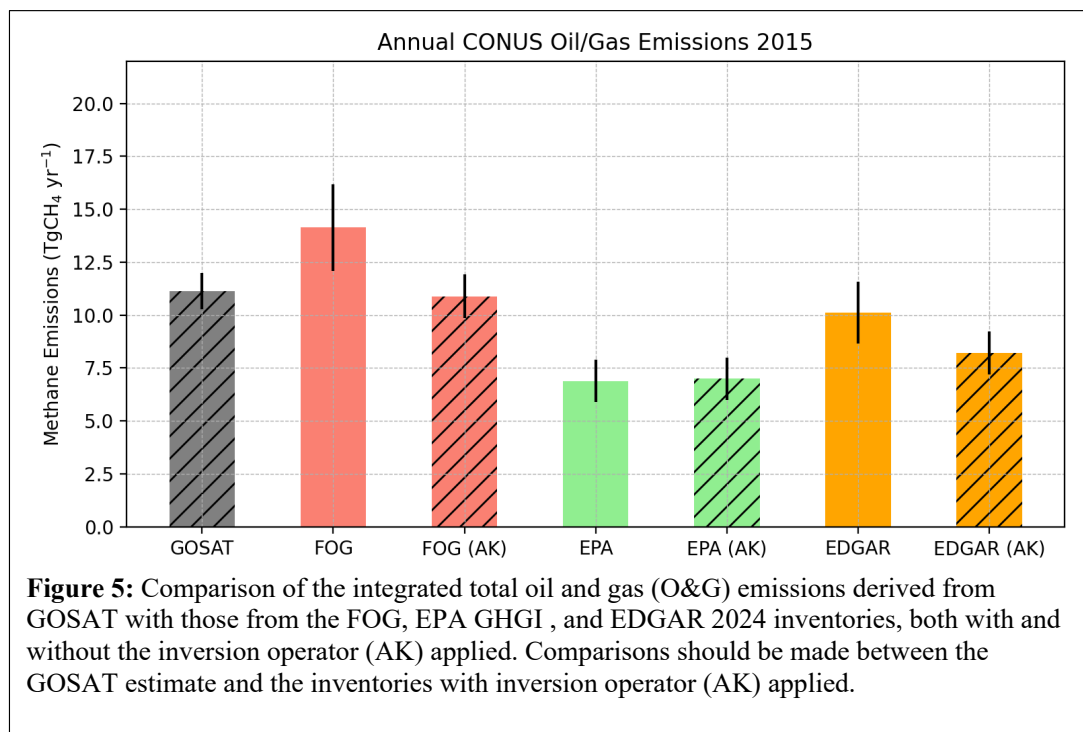


975



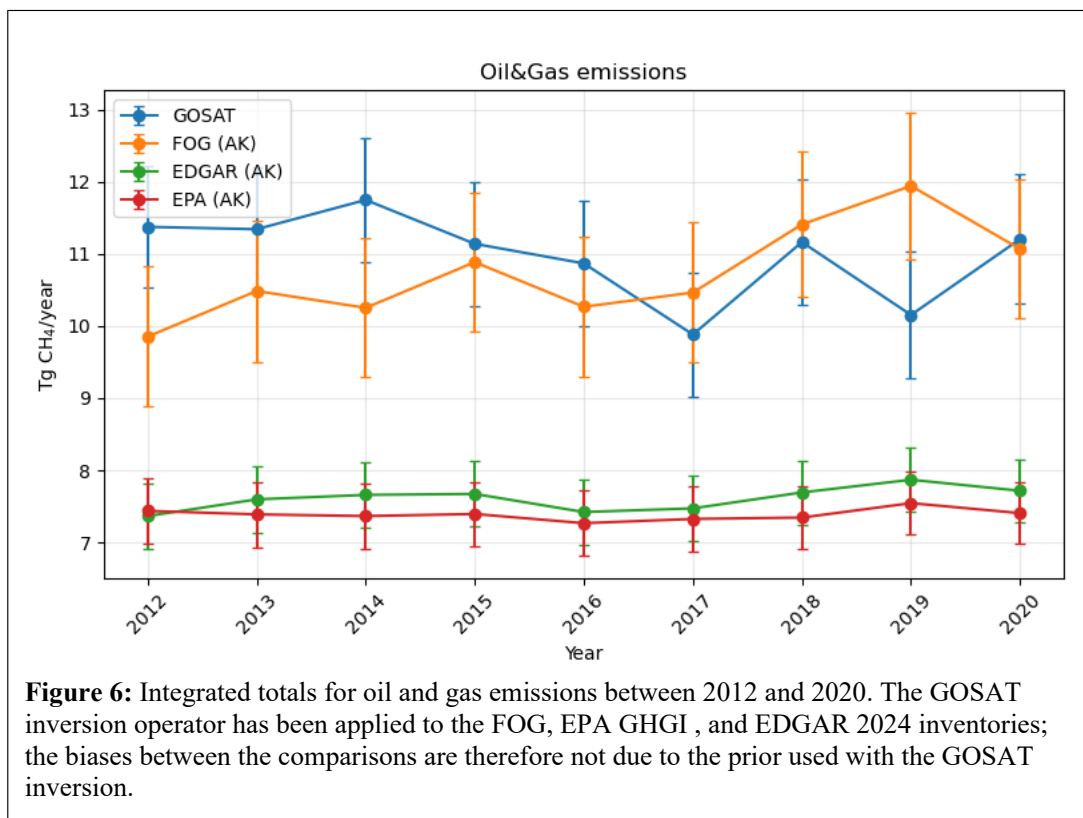


976  
977  
978  
979





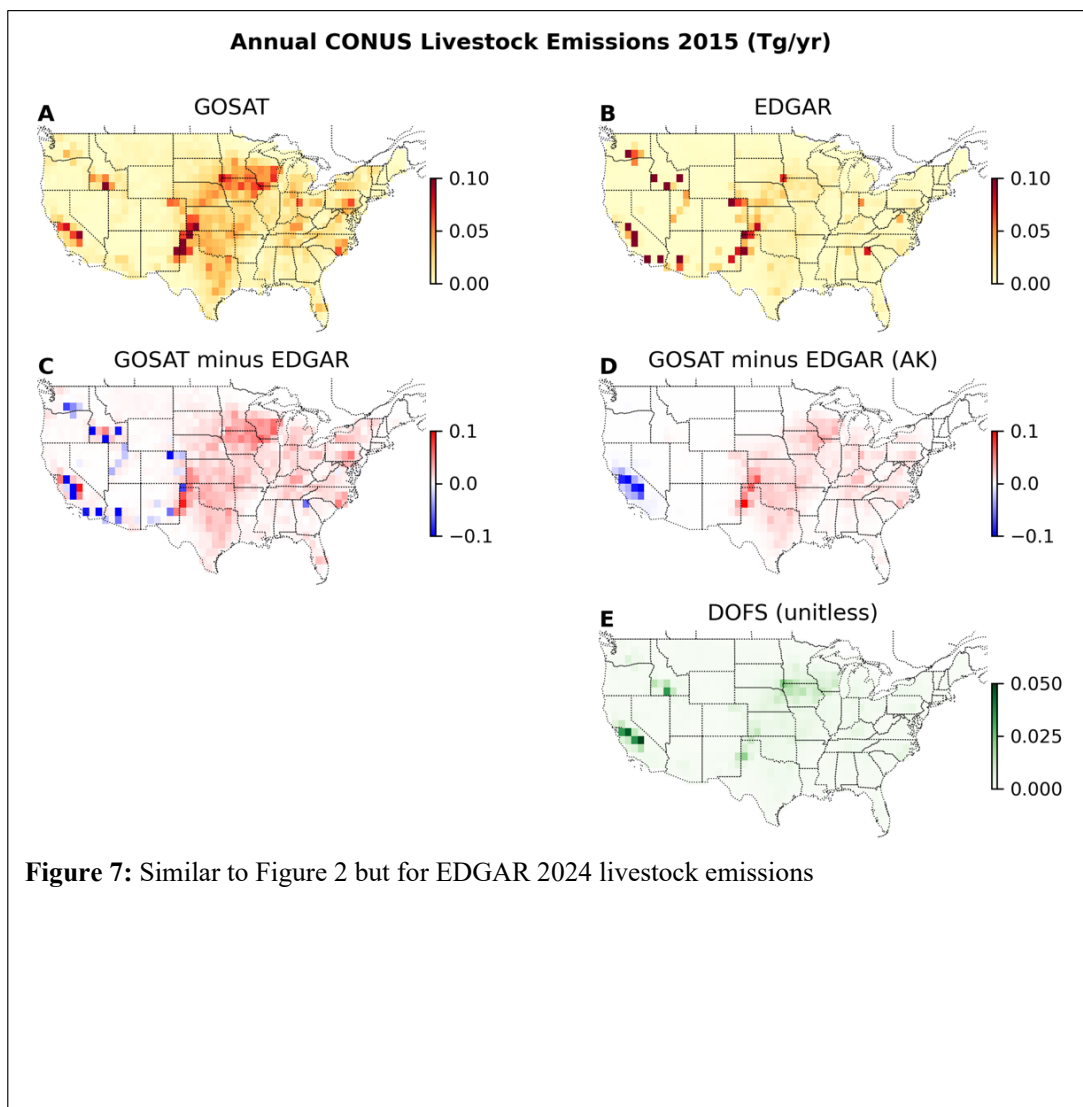
980  
981  
982



983  
984  
985  
986

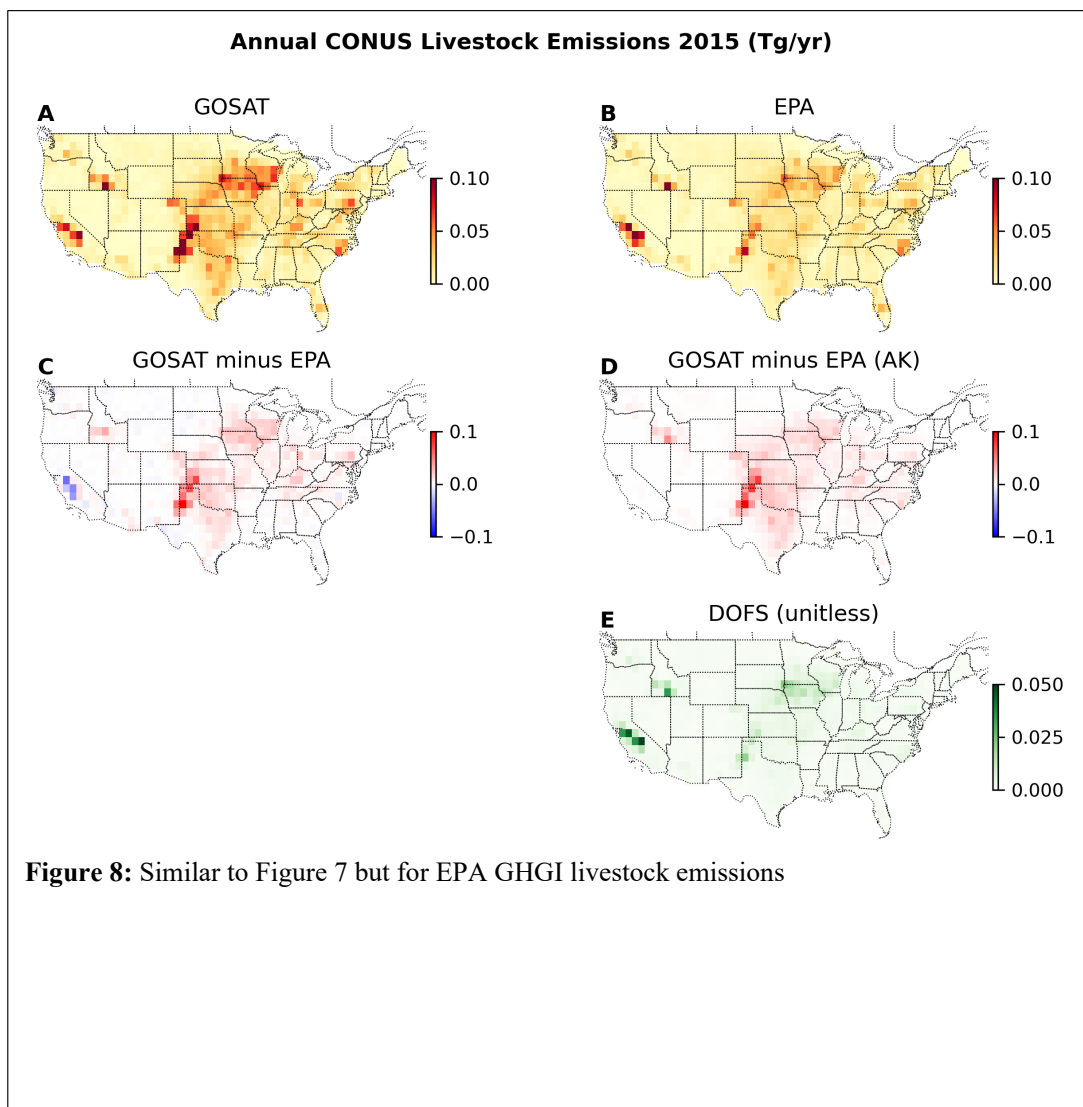


987



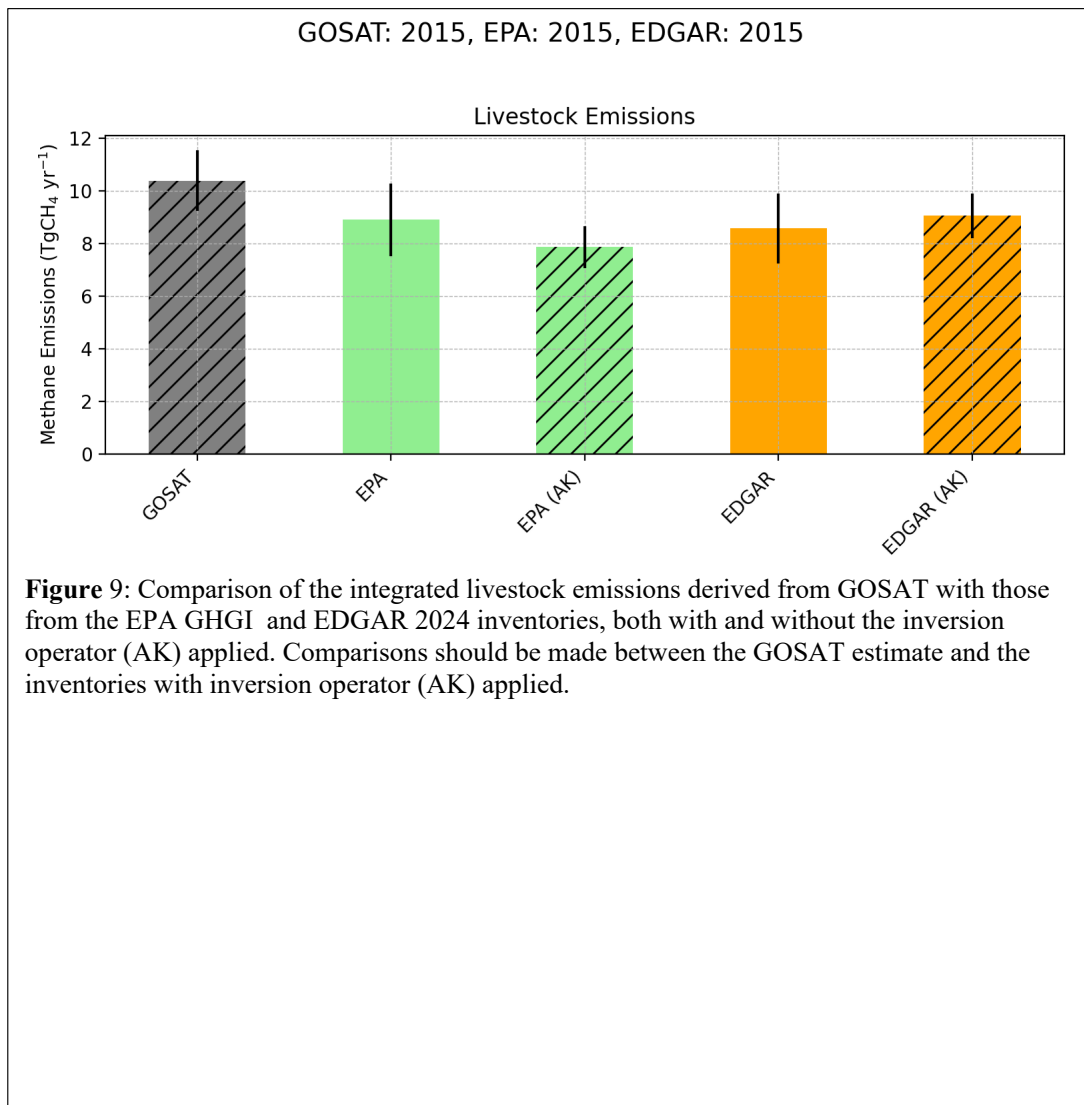


988





989





990  
991  
992  
993  
994  
995

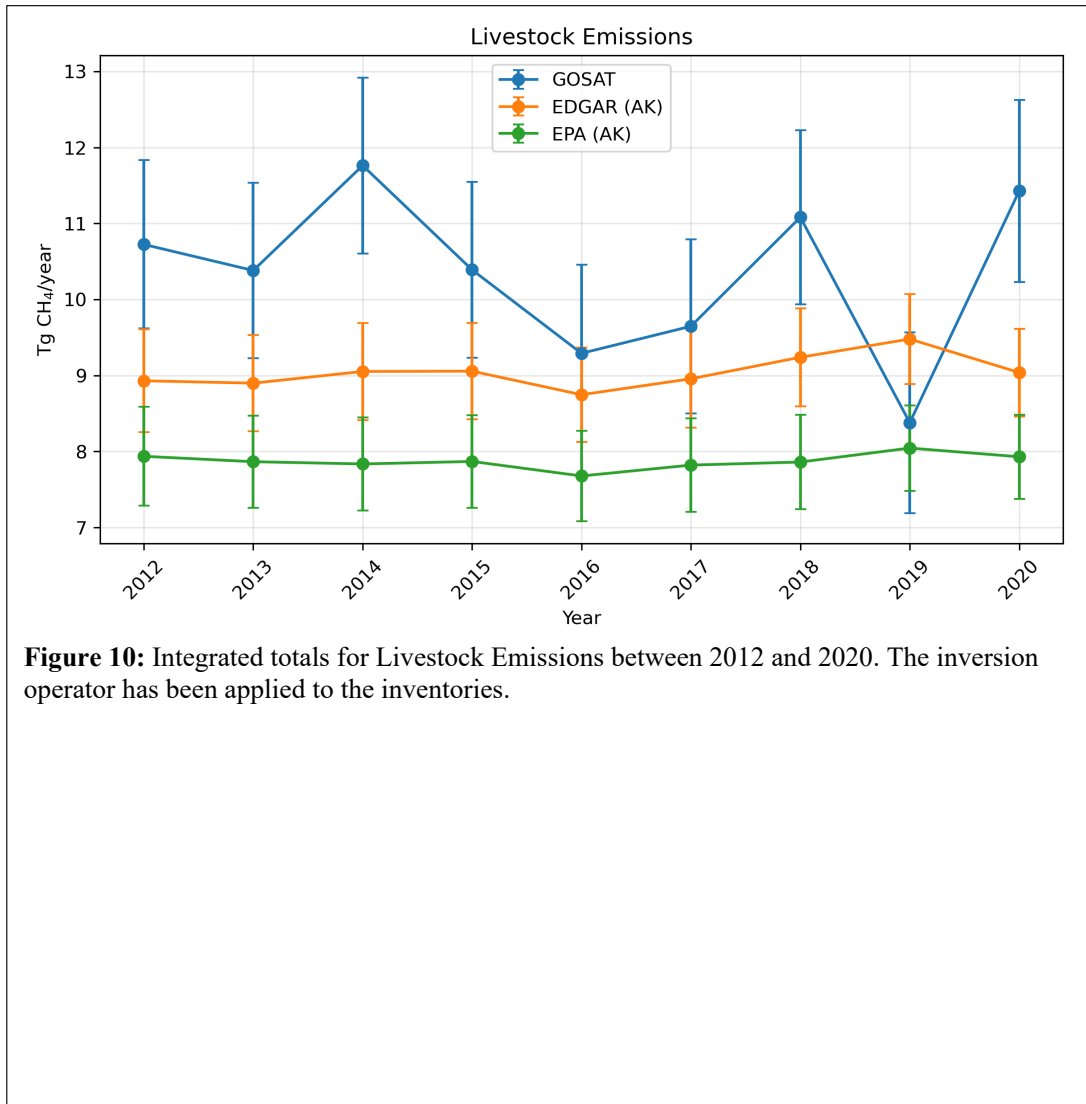


**Figure 10:** Integrated totals for Livestock Emissions between 2012 and 2020. The inversion operator has been applied to the inventories.



996

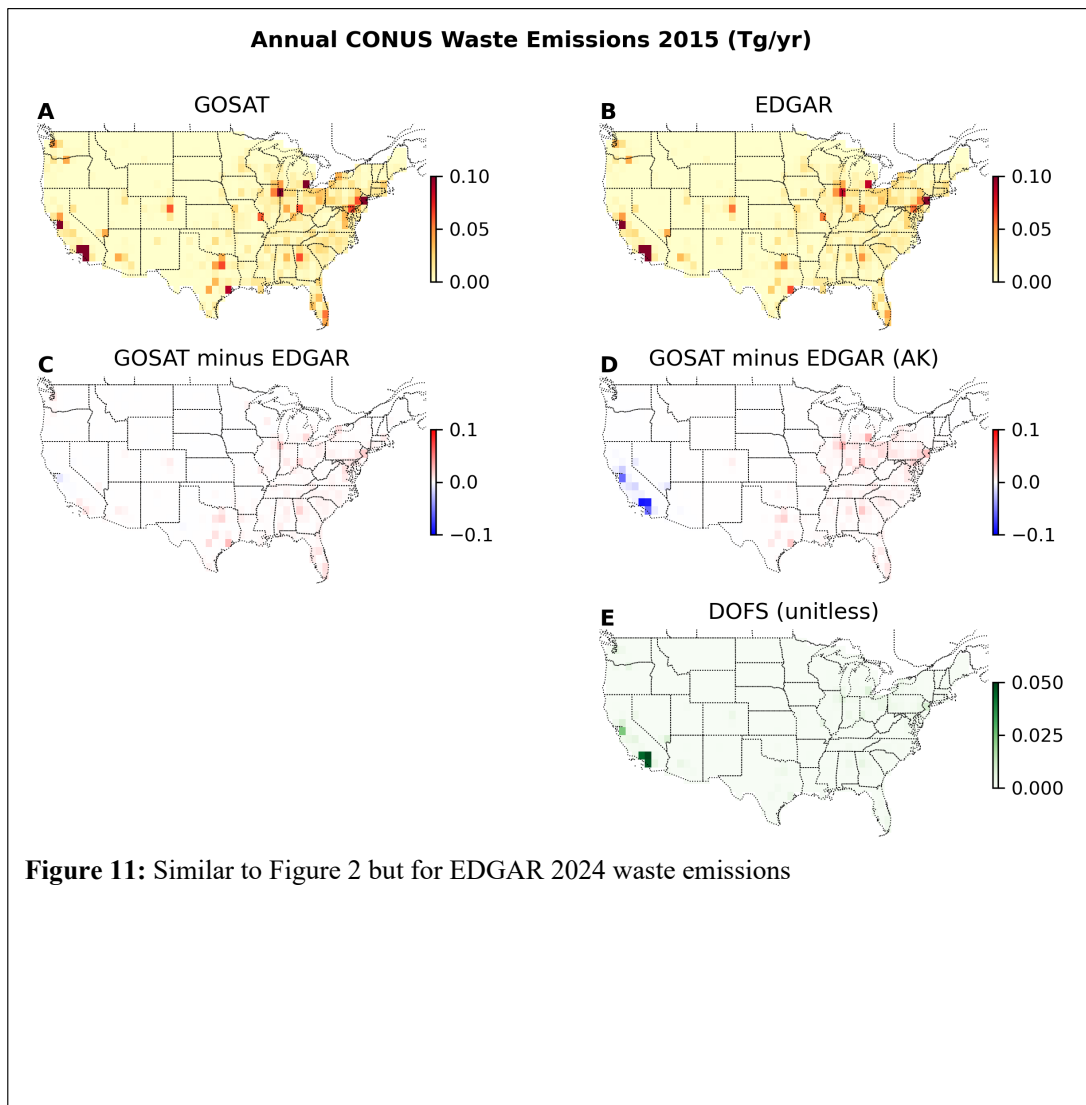
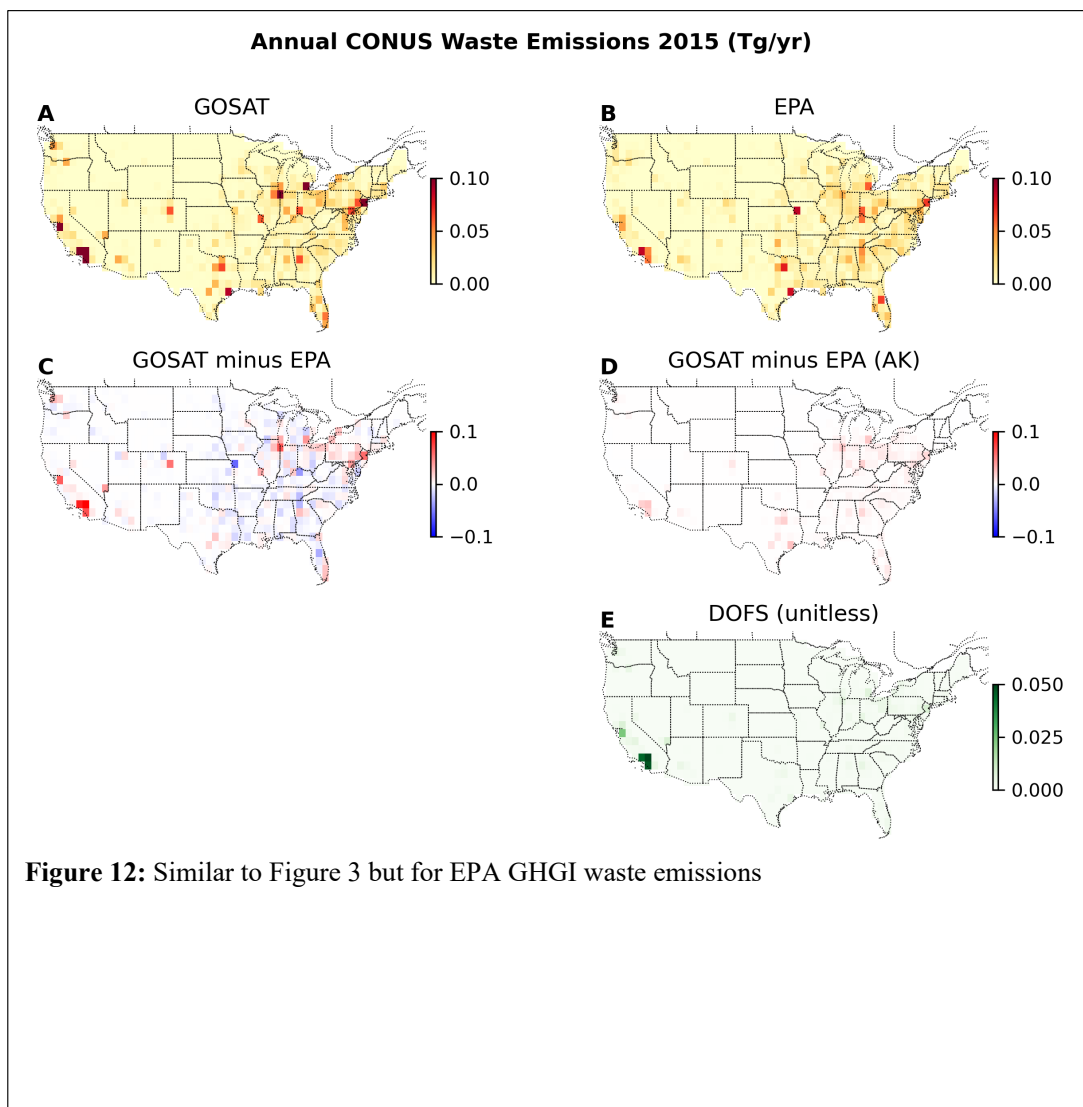


**Figure 11:** Similar to Figure 2 but for EDGAR 2024 waste emissions



997  
998  
999  
1000



1001  
1002  
1003  
1004  
1005  
1006

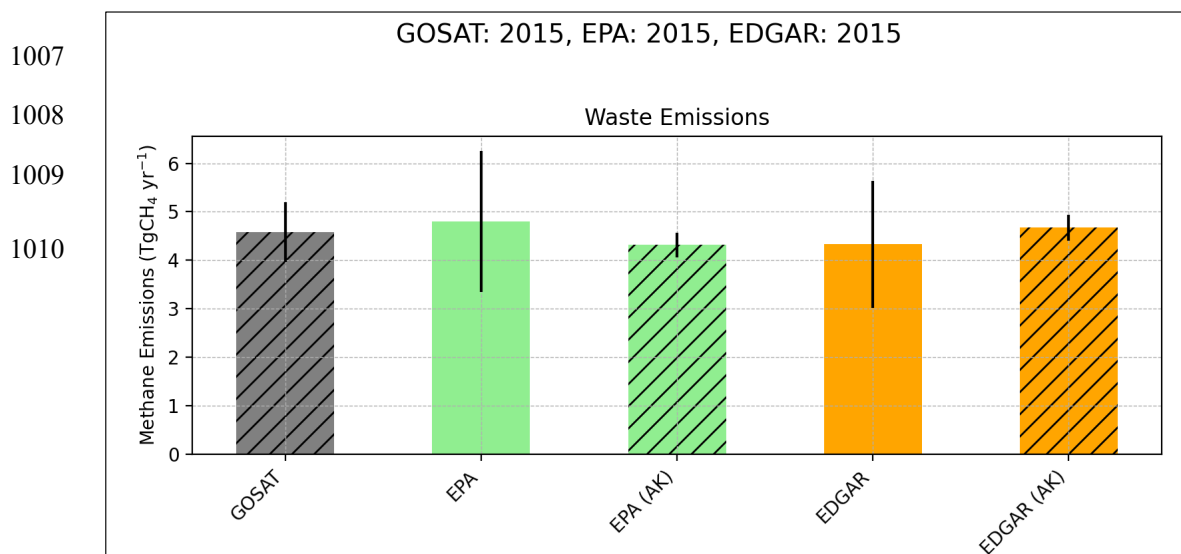


**Figure 13:** Integrated total methane emissions from the waste sector based on GOSAT, along with estimates from the EPA GHGI and EDGAR 2024 inventories, both with and without the inversion operator applied.